Orbital-scale timing and mechanisms driving Late Pleistocene Indo-Asian summer monsoons: Reinterpreting cave speleothem $\delta^{18}{\rm O}$

Steven C. Clemens, Warren L. Prell, and Youbin Sun²

Received 14 January 2010; revised 3 May 2010; accepted 30 June 2010; published 27 October 2010.

Southeast China cave δ^{18} O, often interpreted as a pure East Asian summer monsoon proxy, lags maximum northern hemisphere summer insolation by 2.9 ± 0.3 kyrs at the precession cycle. The Arabian Sea summer monsoon stack lags by 8 ± 1 kyr, consistent with 13 other Indian and East Asian summer monsoon proxies from marine, lake, and terrestrial archives. This 5 kyr phase difference cannot be attributed to age control inadequacies in the marine chronology; it requires reconciliation in the context of proxy interpretation. Both of these lags are incompatible with a direct response to northern hemisphere summer insolation, implicating additional forcing mechanisms. Analysis of heterodynes in the cave δ^{18} O spectrum demonstrates that variance contained in the Arabian Sea summer monsoon proxies also resides in the cave δ^{18} O record. This variance is subtracted from the cave δ^{18} O record yielding a residual that is highly coherent and in phase with precession minima, reflecting the impact of winter temperature change on cave δ^{18} O (meteorological precipitation under cold conditions). Thus, we argue that the timing of light cave δ^{18} O peaks cannot be interpreted as reflecting the timing of strong summer monsoons alone. The 2.9 kyr precession band phase lag of cave δ^{18} O reflects the combined influence of summer monsoon forcing with a phase lag of 8 kyrs relative to precession minima and winter temperature forcing that is in phase with precession minima. This interpretation is consistent with modern seasonality in the amount and isotopic composition of rainfall in southeast China.

Citation: Clemens, S. C., W. L. Prell, and Y. Sun (2010), Orbital-scale timing and mechanisms driving Late Pleistocene Indo-Asian summer monsoons: Reinterpreting cave speleothem δ^{18} O, *Paleoceanography*, 25, PA4207, doi:10.1029/2010PA001926.

1. Introduction

[2] Five high-profile papers have been published on the southeast China cave δ^{18} O records since 2001, having been cited over 600 times. The most recent, Cheng et al. [2009] presents a 390 kyr composite speleothem δ^{18} O record from three caves in southeast China (Hulu, Sanbao, and Linzhu) (Figures 1 and 2a). Wang et al. [2001], Cheng et al. [2006], and Cheng et al. [2009] interpret this cave δ^{18} O as the 'ratio of the amount of summer to winter precipitation' or 'the relative summer to winter monsoon intensities'. Implicit in this interpretation is that the effect of winter monsoon precipitation reaches a minimum when the effect of summer monsoon precipitation reaches a maximum (i.e., they are 180° out of phase). Yuan et al. [2004] interpret cave δ^{18} O as 'the fraction of water vapor removed from air masses between the tropical Indo-Pacific and southeastern China,' a summer monsoon interpretation focused on ocean to land moisture flow. Wang et al. [2008] interpret cave

[3] This summer-centric interpretation is very strongly reflected in the references citing these records. With very few exceptions [Johnson and Ingram, 2004; Maher, 2008] the timing of light cave δ^{18} O is taken to reflect the timing of the strongest summer monsoons, lagging precession minima by 45°, or 2.9 kyrs ($-45^{\circ}/360^{\circ} * 23 \text{ kyrs} = -2.9 \text{ kyrs}$). However, a problem arises when one attempts to reconcile this interpretation of cave δ^{18} O with other summer monsoon proxies from the Indian and East Asian monsoon systems (Figures 1, 2, and A1). These marine and terrestrial proxies indicate that summer monsoon maxima occur significantly later than suggested by the timing of light cave δ^{18} O peaks (-125° or 8 kyrs relative to precession minima). This 80° (5.1 kyr) precession band phase difference is not related to error in the SPECMAP chronology (Text S1 of

Copyright 2010 by the American Geophysical Union. 0883-8305/10/2010PA001926

PA4207 1 of 19

 $[\]delta^{18}{\rm O}$ as reflecting 'changes in summer East Asian monsoon intensity' varying 'dominantly and directly in response to the changes in Northern Hemisphere summer solar radiation at orbital scales.' In all cases, changing strength of the summer monsoon drives the timing of light cave $\delta^{18}{\rm O}$ peaks. Consistent with these summer-centric interpretations, all five papers plot cave $\delta^{18}{\rm O}$ in comparison to northern hemisphere summer radiation curves; none attempt interpretation of the timing or influence of the winter monsoon contribution to the cave $\delta^{18}{\rm O}$ signal independent from that of the summer contribution.

¹Department of Geological Sciences, Brown University, Providence, Rhode Island, USA.

²SKLLQG, Institute of Earth Environment, Chinese Academy of Sciences, Xi'an, China.

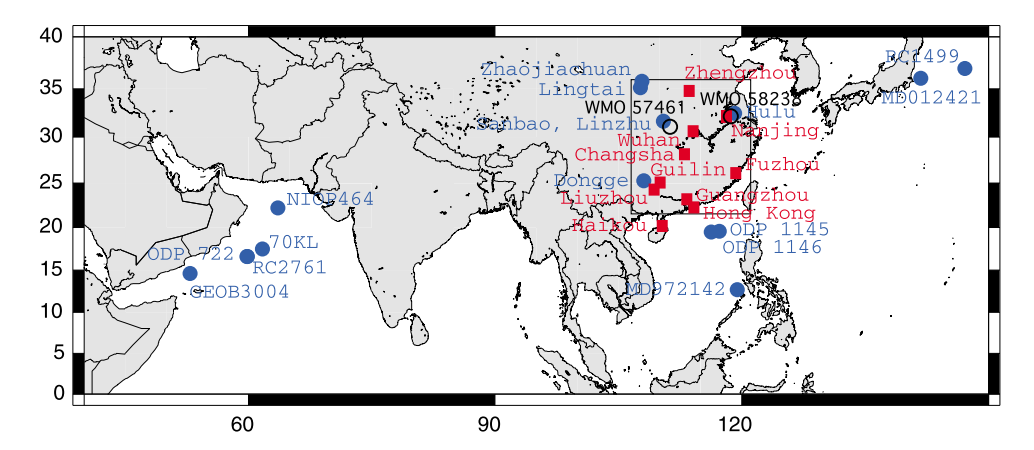


Figure 1. Location map showing marine and terrestrial summer monsoon proxy sites (blue dots), GNIP stations (red boxes), WMO stations (black circles), and the regional southeast China area average (boxed region 21°N to 35°N, 106°E to 122°E). Base map produced at http://www.aquarius.geomar.de/make map.html.

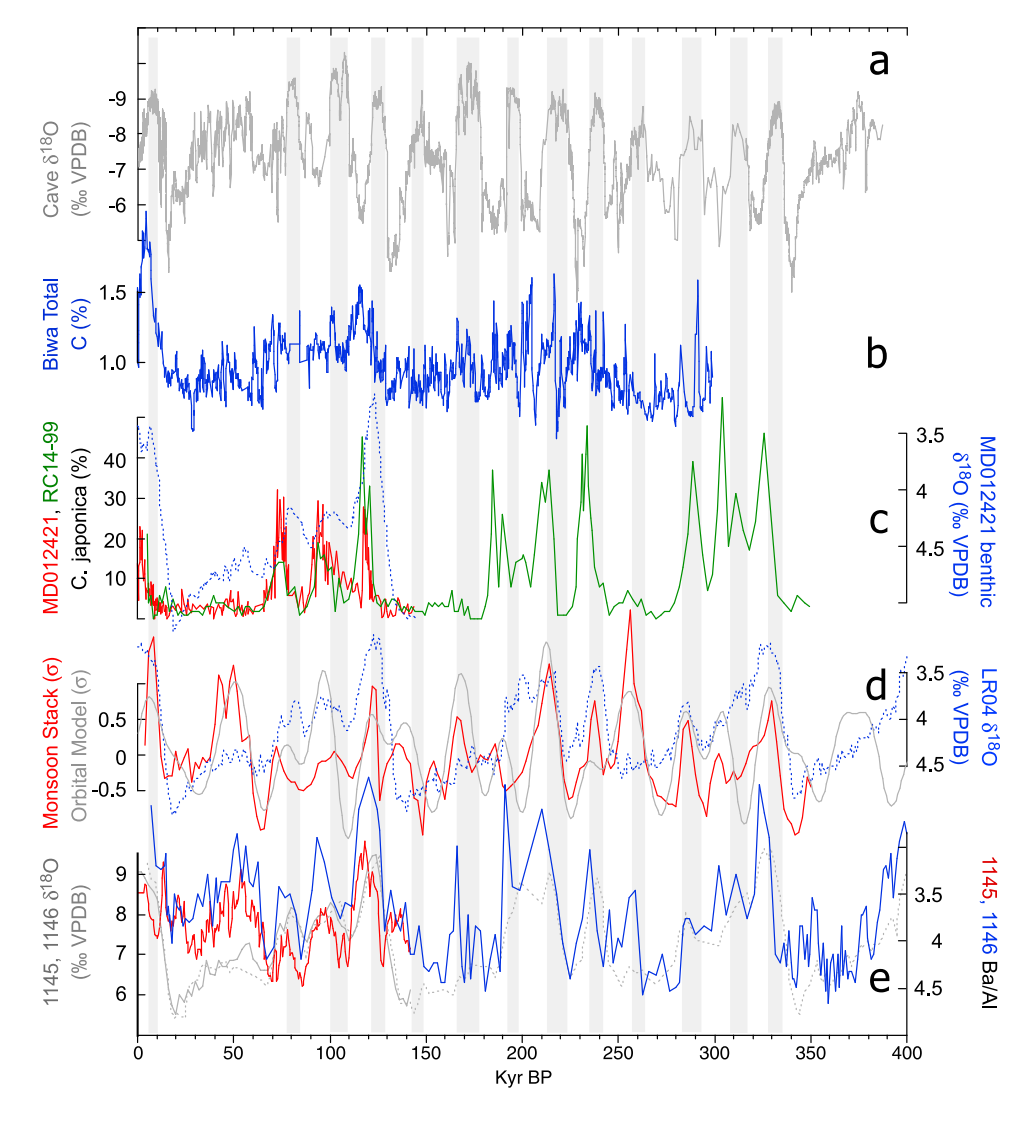


Figure 2. Examples of proxy time series from the Indian and East Asian monsoon regions (Figure 1 and Table A1). Grey shading is centered on light peaks in the cave δ^{18} O record [*Cheng et al.*, 2009]. The timing of peaks in summer monsoon proxies lag light δ^{18} O peaks in the cave record.

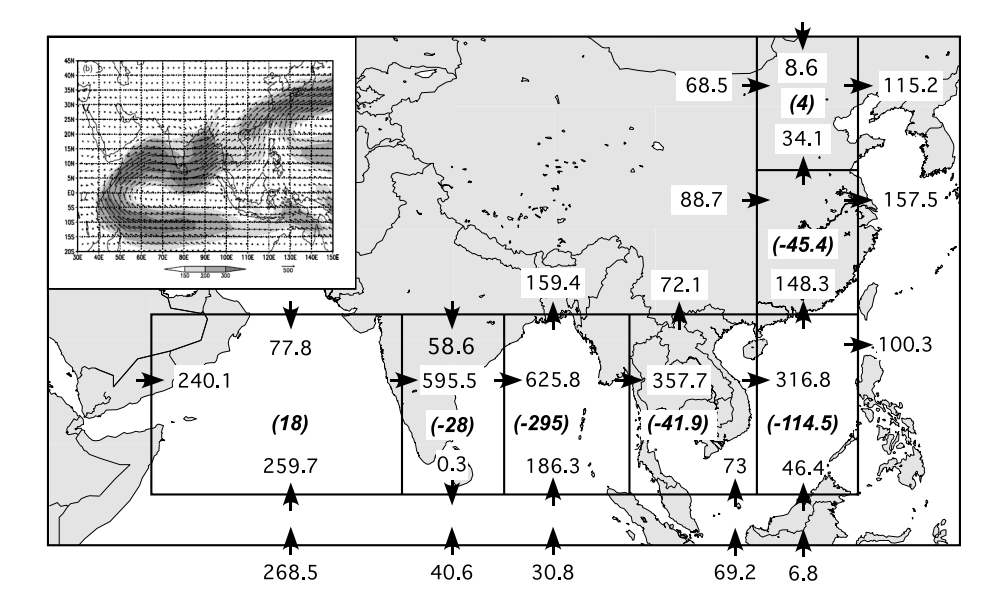


Figure 3. Summer monsoon moisture budget and transport path after *Ding et al.* [2004]. June, July, and August moisture budget averaged for 1990 through 1999. Arrows represent moisture flux across the defined boundaries; units are 10^6 kg s⁻¹. Numbers in parentheses indicate the area to be a net moisture source (positive) our sink (negative). The southern Indian Ocean is the dominant moisture (latent heat) source. India, the Bay of Bengal, IndoChina, the South China Sea, and southeast China are all moisture sinks. (inset) Summer monsoon moisture transport path averaged for 1990 through 1999 (the 5th pentad of May through the 2nd pentad of July; units are kg m⁻¹ s⁻¹). Base map produced at http://www.aquarius.geomar.de/make map.html.

the auxiliary material), requiring reconciliation in terms of proxy interpretation. ¹

[4] We provide an overview of Indian and East Asian climatology as well as summer monsoon moisture sources in section 2. We quantitatively assess the similarities and differences in the cave and Arabian Sea records and the two models proposed to explain them in section 3. In section 4, we leverage the excellent chronology of the cave record to demonstrate that variance observed in the Arabian Sea summer monsoon proxies is present in the cave $\delta^{18}\mathrm{O}$ record as well. In section 5 we remove the Arabian Sea summer monsoon variance from the cave δ^{18} O record and analyze the residuals, showing them to be consistent with a winter temperature forcing, as is evident in modern southeastern China rainfall isotope data. In section 6 we construct a δ^{18} O cave orbital model accounting for the timing of light peaks in cave δ^{18} O as the combined influence of summer monsoon and winter monsoon (temperature) forcing. In section 7, we document that our interpretation of cave δ^{18} O over the past 390 kyrs, as reflecting both summer and winter dynamics, is consistent with modern seasonality in precipitation amount and isotopic composition. Finally, we summarize our results in section 8.

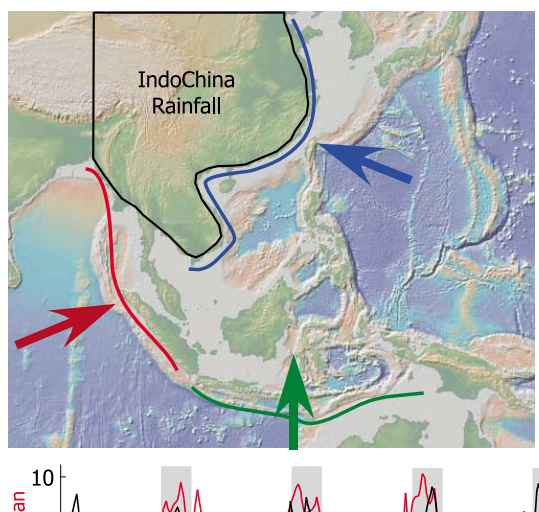
2. Modern Indian and East Asian Climatology

[5] Indian and Asian summer monsoon circulation is initiated by differential sensible heating of continental and oceanic regions, after which cross-equatorial moisture

transport, and the resultant latent heating, plays a dominant role in modulating monsoon strength [Hastenrath and Greischar, 1993; Liu et al., 1994; Loschnigg and Webster, 2000; Webster, 1987, 1994; Webster et al., 1998; Yanai and Tomita, 1998]. If only direct sensible heating were important, the monsoon would be weaker, with little or no variability on interannual and longer time scales. Modern meteorological observations and moisture transport budgets (Figure 3) quantitatively show that the southern hemisphere (SH) Indian Ocean is the dominant source of moisture (latent heat) to the Indian and East Asian summer monsoons during June, July, and August (JJA) [Bosilovich and Schubert, 2002; Ding et al., 2004; Ding and Chan, 2005; Emile-Geay et al., 2003; Liu and Tang, 2004, 2005; Park et al., 2007; Simmonds et al., 1999; Wajsowicz and Schopf, 2001; Zhu and Newell, 1998]. The moisture budget shows that the Arabian Sea is a minor moisture source while the Bay of Bengal, IndoChina, the South China Sea, and southeastern China are all moisture sinks. At this scale, the Pacific Ocean contributes relatively little moisture to the summer monsoon system during June, July, and August.

[6] Satellite scatterometer-based moisture budgets support these findings (Figure 4), showing that June, July, and August (JJA) rainfall in IndoChina is coherent and in phase with JJA moisture transport from the Indian Ocean but out of phase with that from the Pacific [Liu and Tang, 2004]. These modern dynamics strongly suggest that paleomonsoon records should be interpreted with southern hemisphere Indian Ocean dynamics in mind [Clemens and Prell, 2003; Liu et al., 2006; Rohling et al., 2009] and

 $^{^1\}mathrm{Auxiliary}$ materials are available in the HTML. doi:10.1029/2010PA001926.



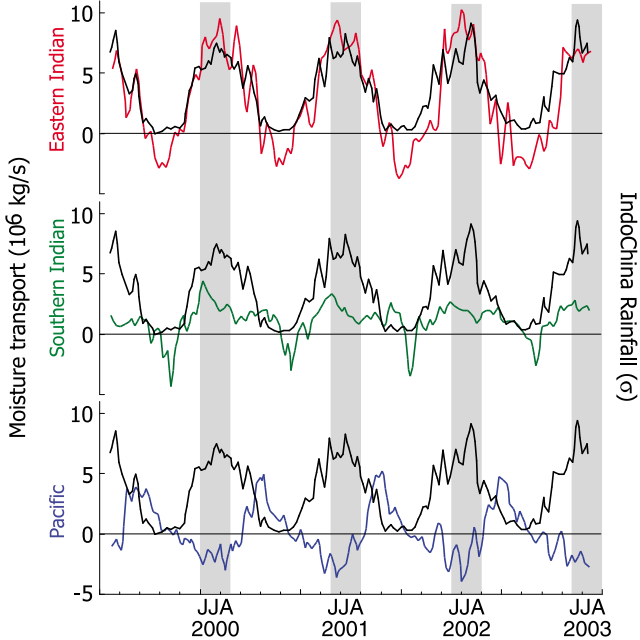


Figure 4. Satellite scatterometer-based moisture transport from August 1999 to August 2003. Moisture transport from the eastern Indian Ocean (across the red boundary) and the southern Indian Ocean (across the green boundary) is in phase with rainfall in IndoChina (Black time series in all three plots). In contrast, moisture transport from the Pacific Ocean (across the blue boundary) is out of phase with rainfall in IndoChina. These data indicate that summer monsoon rainfall in IndoChina is dominantly sourced from the Indian Ocean, not the Pacific. Redrawn from *Liu and Tang* [2004]. Base map produced using GeoMapApp http://www.geomapapp.org/supported by the National Science Foundation.

that the Indian and East Asian summer monsoon systems are linked through a common, Indian Ocean moisture source.

3. Phase of Cave δ^{18} O and Arabian Sea Proxies Relative to Orbital Forcing

[7] The importance of establishing an appropriate reference point for measuring the phase of climate proxies rel-

ative to insolation forcing lies in the concept that phase is a key indicator of the degree to which a proxy does or does not respond directly to insolation forcing. For example, if the summer monsoon responds only to the degree of sensible heating over Asia, then monsoon maxima should have a zero-phase relationship with the maximum insolation forcing. As demonstrated in section 3.2, both the Arabian Sea and Cave $\delta^{18}{\rm O}$ proxies significantly lag maximum northern hemisphere insolation at the precession band. A significant lag reflects either a large response time or that one or more additional forcing mechanisms are involved in determining the timing of the maximum response. Given that the monsoon is a fast–physics surface system, we argue that the 45° lag of the cave record reflects multiple forcing mechanisms.

3.1. Establishing a Reference Point for Phase Measurement

[8] Figures 5a and 5b show plots of cave δ^{18} O and the Arabian Sea summer monsoon stack (SM stack) relative to ETP [Cheng et al., 2009; Clemens and Prell, 2003]. ETP is constructed by normalizing and stacking eccentricity, tilt (obliquity) and negative precession yielding a single convenient record against which proxy time series can be spectrally compared in order to evaluate coherence and phase (timing) relative to orbital extremes [Imbrie et al., 1984] (Figures 5c and 5d). Cross-spectral results are plotted on phase wheels (Figures 5e and 5f). Zero on the obliquity phase wheel is set at maximum obliquity while zero on the precession phase wheel is set at precession minimum; both orbital configurations denote the timing of warmest northern hemisphere summers and coldest northern hemisphere winters (at latitudes poleward of 22.5°N). Minimum precession represents the specific orbital configuration when the Earth is at perihelion and the North Pole is pointed directly at the Sun. This configuration is commonly referred to as '21 June' perihelion or, more appropriately $\omega =$ 90°, where ω (ω ° in the work by Berger [1978]) is the longitude of perihelion relative to the moving vernal equinox of 1950 AD [Berger, 1978]. Considering the full precession cycle, no other orbital configuration exists for which insolation maxima are stronger during northern hemisphere summer nor insolation minima weaker during northern hemisphere winter (at latitudes poleward of 22.5°N). Thus, minimum precession and maximum obliquity are natural reference points for measuring the phase of the Indo-Asian summer and winter monsoons. This point is confirmed by examining absolute annual maximum and minimum insolation curves calculated following *Huybers* [2006].

[9] Unlike insolation curves typically plotted with paleomonsoon records (e.g., '21 June' $\omega=90^\circ$, '21 July' $\omega=120^\circ$, 'JJA' average of $\omega=90^\circ$, 120° and 150°), absolute annual maximum (or minimum) insolation curves are not tied to any specific orbital configuration but, rather, indicate the absolute maximum (or minimum) radiation received at a given latitude and time in the past, regardless of orbital configuration. Absolute maximum radiation for 30°N, the latitude of the cave δ^{18} O composite, is shown in Figure 6a. At the 23,000 year precession time scale, absolute isolation maxima always fall in the month of June, coincident with

 $\omega=90^\circ$. However, at the annual time scale, when precession is changing from $\omega=270^\circ$ toward $\omega=90^\circ$, absolute insolation maxima very often occur when perihelion takes place in May. Similarly, when precession is changing from $\omega=90^\circ$ toward $\omega=270^\circ$, absolute insolation maxima frequently occur when perihelion takes place in July. Both early and late season insolation maxima are important in driving changes in overall summer monsoon strength.

[10] The absolute maximum 30°N insolation curve (Figure 6a) incorporates the maximum radiation received over time, regardless of orbital configuration. In contrast, the JJA curve never yields the maximum insolation value received at 30°N (Figure 6b). Radiation received in the month of July accounts for the absolute annual maximum only 29% of the time over the past 400 kyrs whereas radiation received in June accounts for the maximum 59% of the time. At 30°N, the absolute maximum curve ranges between 5 and 60 w/m² greater than the commonly used JJA insolation reference curve. For example, at 225 ka, the classic JJA curve indicates insolation forcing of 457 w/m² whereas the maximum radiation actually experienced is 514 w/m² (Figure 6b). In fact, the maximum radiation in April, May, and June are all three greater than indicated by the JJA and 21 July curves (Figure 6b). The fact that summer (southwest) monsoon winds in the northern Arabian Sea are established in May (Figure 7) underscores the importance of taking into account early season heating in terms of overall strengthening and/or longer duration summer monsoons. In the same vein, late summer insolation maxima (July) also strengthen and/or prolong the summer monsoon.

[11] Invoking insolation curves tied to specific orbital configurations may not be appropriate in that none reflect the true magnitude or timing of maximum insolation received at a specific times in the past (Figure 6b). Choosing a curve on the basis that it matches the phase of a given proxy may also be, in this light, inappropriate. For example, the cave record, which has a phase of -45° , should be compared to the 6 August insolation curve ($\omega = 90 + 45 = 135^{\circ}$). The 6 August insolation at 225 Ka was 427 w/m², a full 87 w/m² less than the strongest insolation actually experienced that year at 30°N.

[12] In summary, we submit that the absolute maximum insolation curve is the most appropriate reference for comparison with summer monsoon records. This approach yields the absolute maximum radiation received at a given latitude through time regardless whether it occurs in late spring, summer, or early fall, accounting for early onset or late retreat of monsoonal circulation. Any significant deviation from zero phase implicates additional forcing mechanisms beyond direct responses to maximum sensible heating.

3.2. Precession and Obliquity Band Phase Responses

[13] The cave and SM stack both have 23 kyr spectral peaks that are very strongly coherent with precession (Figures 5c and 5d). Light cave δ^{18} O lags absolute maximum precession-driven insolation (and precession minima) by $45 \pm 2^{\circ}$. The SM stack lags by $123 \pm 12^{\circ}$. The SM stack is strongly coherent and, within error, in phase with absolute maximum obliquity-driven insolation and obliquity maxima

 $(-13 \pm 14^{\circ})$. Cave δ^{18} O, in contrast, has two distinct non-primary spectral peaks at 52.6 kyr and 35 kyr periods, masking any 41 kyr variance in cave δ^{18} O. The larger of these nonprimary spectral peaks represents the heterodyne of obliquity and the 23 kyr component of precession $(1/41 \pm 1/23 = 1/14.7$ and 1/52.4) while the smaller represents the heterodyne of obliquity and the 19 kyr component of precession $(1/41 \pm 1/19 = 1/13)$ and 1/35.4) We address these important spectral peaks further in section 4, after a review of the current conceptual models developed to explain the cave δ^{18} O and Arabian Sea SM stack records in the context of monsoon forcing.

3.3. Conceptual Models for Mechanisms Driving Cave $\delta^{18}{\rm O}$ and Arabian Sea Proxies

[14] Wang et al. [2008] interpret cave δ^{18} O as reflecting 'changes in summer East Asian monsoon intensity' varying 'dominantly and directly in response to the changes in Northern Hemisphere summer solar radiation at orbital scales.' For all practical purposes, this is no different from the explanations of Wang et al. [2001], Cheng et al. [2006], and Cheng et al. [2009], who interpret cave δ^{18} O as the ratio of the amount of summer to winter precipitation, with the implicit assumption that when the effect of the summer monsoon is strong, the effect of the winter monsoon is weak (180° out of phase). All interpret the timing of cave δ^{18} O minima as times of strongest summer monsoons. None attempt interpretation of the winter monsoon influence on cave δ^{18} O independent from that of the summer influence, particularly with regard to phase.

[15] This summer insolation forcing model cannot explain the $45^{\circ} \pm 2^{\circ}$ lag relative to precession minima and absolute maximum summer insolation forcing. The interpretation of the 45° lag as a response to 21 July, JJA, or for that matter, 6 August insolation forcing, is not consistent with results from time-dependent, fully coupled model experiments simulating the monsoon response to insolation-only forcing at the orbital scale. Kutzbach et al. [2007] find that Asian summer monsoon precipitation (JJA) leads precession minima by 23°, a full 68° prior to the timing of light cave δ^{18} O at the precession band [see Kutzbach et al., 2007, Table 2 and Figures 4a and 5]. Similarly, *Tuenter et al.* [2005] find that June and July precipitation lead precession minima by 2200 and 500 years, respectively, while August precipitation lags precession mimima by 1900 years. This yields a combined JJA lead of 800 years or 12°. This 12° JJA precipitation lead is comparable to the 23° lead in the Kutzbach et al., experiment. In other words, if the late Pleistocene monsoon responded only to summer insolation forcing, these model results indicate that JJA precipitation maxima should lead precession minima (and the maximum insolation forcing) by 12° to 23°, not lag it by 45°. On this basis, we contend that the 45° cave δ^{18} O lag is not consistent with a direct response to summer insolation forcing and that additional mechanisms must be involved.

[16] In sections 4–6, we make the case that the timing of light cave δ^{18} O is the result of (1) a summer monsoon forcing as indicated by the Arabian Sea SM stack and (2) a

winter monsoon temperature influence. First, however, we describe the conceptual model for the Arabian Sea proxies.

[17] The model explaining the Arabian Sea summer monsoon in the context of orbital forcing follows *Clemens and Prell* [2003]. The –123° precession band phase of the SM stack is interpreted in terms of the summer monsoon responding to three mechanisms, northern hemisphere summer insolation, minimum ice volume conditions, and the maximum export of latent heat from the southern subtropical Indian Ocean. Northern hemisphere summer insolation (differential land-ocean sensible heating) initiates summer monsoon flow. Recent time-dependent experiments with a

fully coupled Fast Ocean Atmosphere Model (FOAM) forced only by insolation have demonstrated that NH summer insolation is sufficient to initiate cross-equatorial flow at all orbital configurations [Kutzbach et al., 2007]. Within each seasonal cycle, we view this mechanism as initiating cross-equatorial flow. However, at the precession scale the Arabian Sea proxy records indicate maxima at -123°, between ice volume minima (-78°) and precession maxima (-180°). This is interpreted as indicating that the timing of strong summer monsoons at this orbital scale is sensitive to extremes in these two mechanisms (Figure 5e).

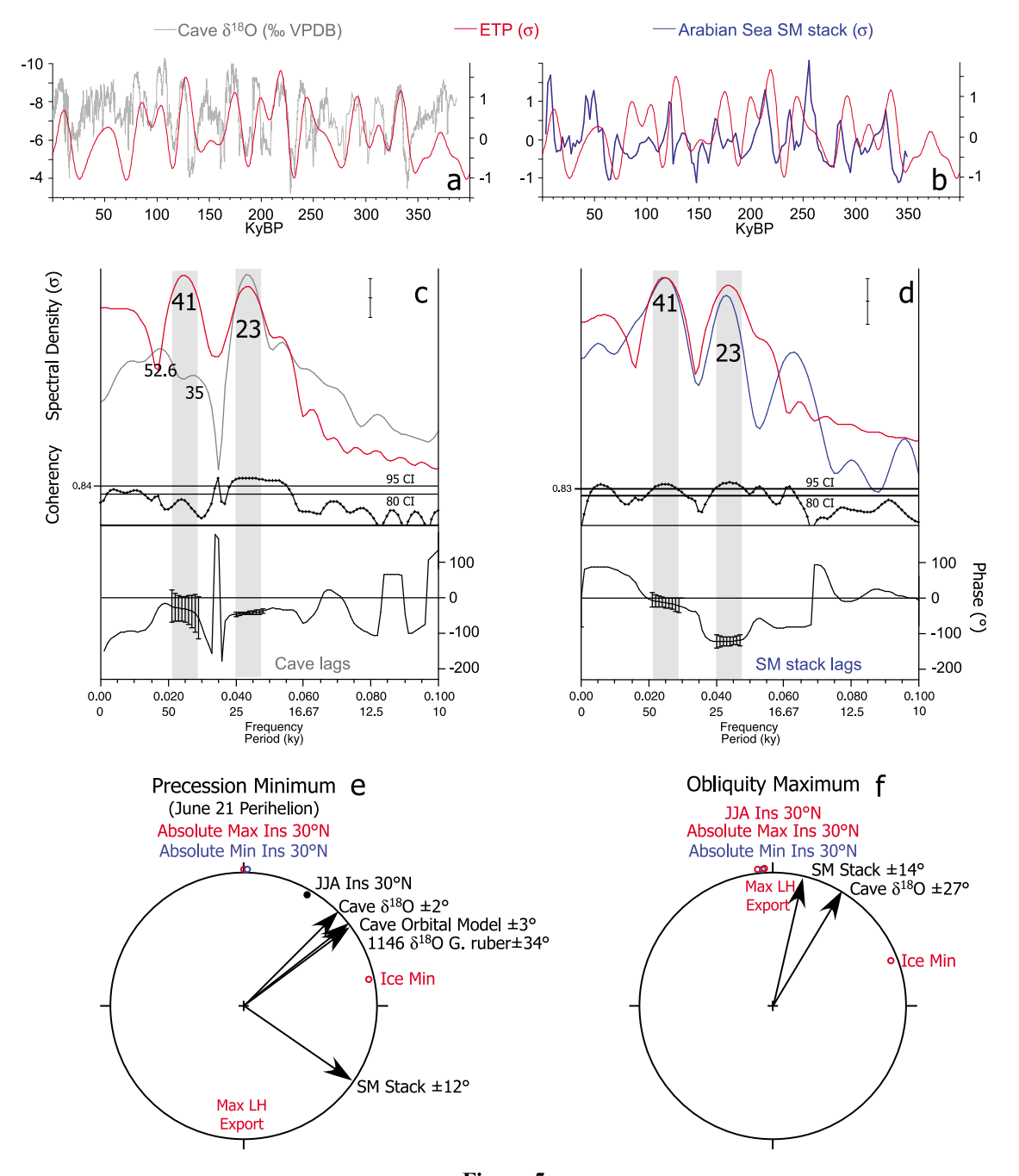


Figure 5

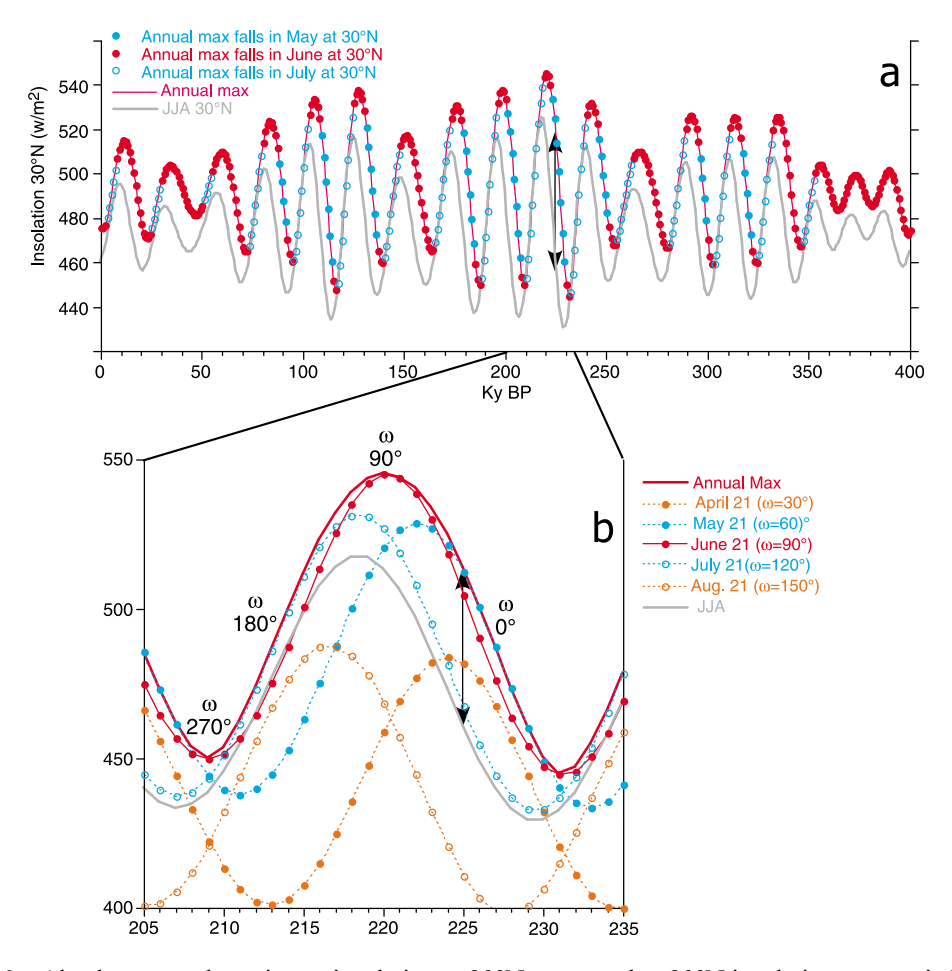


Figure 6. Absolute annual maximum insolation at 30°N compared to 30°N insolation curves tied to specific orbital configurations (e.g., '21 July insolation' or 'JJA insolation'). Absolute maximum insolation curves are not tied to specific orbital configurations. Rather, they yield the absolute maximum insolation at a given latitude and time in the past regardless of whether it occurs in late spring, summer, or early fall.

[18] General circulation models have typically shown a tendency toward decreased monsoon strength under glacial conditions [Barnett et al., 1989; Prell and Kutzbach, 1987, 1992] with the implication that minimal glacial boundary conditions (-78°) favor strengthened monsoons. Maximum precession (-180°) is interpreted as the time within the

precession cycle where the export of latent heat from the southern subtropical Indian Ocean is maximized [Clemens and Prell, 2003]. At precession maxima (21 December perihelion, $\omega = 270^{\circ}$) SH summer (DJF) is characterized by maximum insolation, resulting in the storage of heat in the ocean mixed layer. This is followed by SH winter (JJA),

Figure 5. (a and b) Time series, (c and d) cross spectra, and (e and f) phase wheels comparing cave δ^{18} O and the Arabian Sea summer monsoon stack to Earth orbital parameters (ETP). ETP is a combined record of normalized eccentricity, obliquity (tilt), and negative precession ($\omega = 90^{\circ}$, 21 June perihelion) [Laskar et al., 1993]. Precession is defined as $\Delta e \sin \omega$ where ω is the longitude of perihelion measured from the moving vernal equinox (referenced to 1950 AD), and e is the eccentricity of Earth's orbit about the Sun [Berger, 1977; Laskar et al., 1993]. Periods (1/frequency) of the main spectral peaks are labeled. Spectral densities are normalized and plotted on log scales. The horizontal lines on the coherence plot indicate the 80% and 95% confidence intervals (CI). Additional details on cross-spectral methods are given in Appendix A. Zero points on the phase wheels are set at precession minimum (Pmin, $\omega = 90^{\circ}$, 21 June perihelion) and obliquity maximum. Negative phase values are measured in the clockwise direction representing temporal lags. For example, δ^{18} O minima (Ice Min) have a phase of -78° relative to precession minima indicating a 5000 year lag ($-78^{\circ}/360^{\circ} \times 23,000$ years). The timing of potential summer monsoon forcing mechanisms are denoted by red text including the absolute maximum insolation over Asia in summer [Prell and Kutzbach, 1992], δ^{18} O minima (Ice Min) [Prell and Kutzbach, 1992], and maximum export of latent heat from the southern subtropical Indian Ocean (-180° at the precession band and 0° at the obliquity band) [Clemens and Prell, 2003; Liu et al., 2006]. The timing of minimum winter insolation over Asia is denoted by blue text.

NCEP/NCAR Reanalysis 1000mb Vector Wind (m/s) composite Mean May: 1970 to 2008

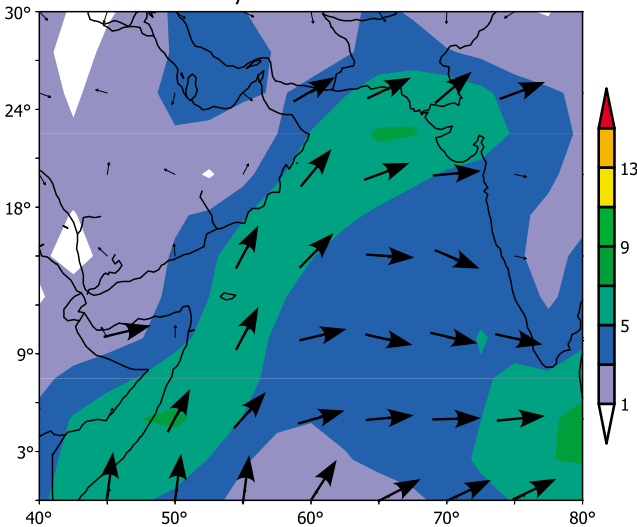


Figure 7. NCAR/NCEP vector winds showing that the southwest summer monsoon winds are established in May. Strong early season insolation contributes to stronger and longer summer monsoon seasons.

characterized by minimum insolation, yielding a cold (dry) atmosphere over a warm ocean thus maximizing latent heat export. Liu et al. [2006] tested this hypothesis using two fully coupled ocean-atmosphere GCM experiments in which insolation was increased in the SH during SH summer (December to April) and in the NH during NH summer (May to September), monitoring the resulting effect on boreal summer monsoon (JJA) precipitation over South Asia. Increased NH summer insolation had an immediate and positive impact on summer monsoon (JJA) precipitation over South Asia. However, the increased SH summer insolation experiment had 10% larger impact on subsequent summer monsoon (JJA) precipitation over South Asia. These experiments support the interpretation that the timing of latent heat export is part of the reason why the Indo-Asian summer monsoon has a phase of -123°. However, model proxy discrepancies do exist. For example, the increased model precipitation is not accompanied by increased model wind strength whereas the Arabian Sea proxy data indicate strengthened wind-driven upwelling.

[19] In summary, the -123° phase suggests that differential sensible heating initiates summer monsoon flow whereas the timing of summer monsoon maxima at the precession band are sensitive to the timing of ice volume minima [Prell and Kutzbach, 1992] and the export of latent heat from the southern subtropical Indian ocean [Clemens and Prell, 2003; Liu et al., 2006]. A multiproxy synthesis of 19 SM records (Appendix A) yields a precession band phase of $-125^{\circ} \pm 17^{\circ}$ and confirms this phase response as common to marine and terrestrial records spanning the Indian and East Asian regions. We provide evidence in Figure S1 of the auxiliary material demonstrating that this large precession band phase difference relative to that of the cave δ^{18} O

record $(-125^{\circ} \text{ versus } -45^{\circ})$ is not related to error in the SPECMAP chronology.

[20] Unlike the cave δ^{18} O spectrum, the SM stack spectrum indicates distinct, coherent variance in the obliquity band, roughly equal in proportion to that in the precession band (Figure 5d). Importantly, the same latent and sensible heat mechanisms discussed for the precession band also apply at the obliquity band [Clemens and Prell, 2003]. In this case, however, both maximum sensible heating and maximum latent heating occur at obliquity maxima, accounting for the large concentration of variance at the obliquity band (Figures 5d and 5f). Thus, the sensible and latent heat mechanisms are found to operate similarly in both orbital bands, adding considerable internal consistency to the interpretation of mechanisms driving the timing of strong summer monsoons at Earth's orbital time scales.

[21] A simple orbital model for the timing of strong summer monsoons can be constructed as the sum of obliquity (O) with no lag and precession minima with a lag of -125° or 8 kyrs (Pmin_{lag8}). This orbital model is plotted in Figure 2e. This model interprets SM strength in the context of insolation, ice volume, and latent heating and is in contrast to interpretation of the SM as responding only to NH summer insolation.

[22] We next demonstrate that the cave δ^{18} O and the SM stack are significantly coherent with one another at both the obliquity and precession bands indicating that the variance in the SM stack is contained in the cave δ^{18} O record as well. We then remove this summer monsoon signal from the cave δ^{18} O record and analyze the residual record, showing it to be consistent with a winter forcing.

4. Using Heterodynes to Establish the Link Between the SM Stack and Cave δ^{18} O

[23] Cross spectra between cave δ^{18} O and the SM stack documents coherence (>95 CI) at the precession band (Figure 8a). Interestingly, coherence and near-zero phase is also indicated at the 41 kyr obliquity band although the implied 41 kyr spectral peak is masked by the nonprimary peaks to either side. Narrow 41 kyr band-pass filters of the two records illustrate the coherence at the 41 kyr band implied by the cross spectrum (Figure 8b). Thus we plot the phase of cave $\delta^{18}O$ on the obliquity phase wheel relative to the SM stack (Figure 5f) acknowledging that the concentration of obliquity variance in cave $\delta^{18}{\rm O}$ is small. These cross spectral and band-pass-filter results document that variance contained within the SM stack resides within the cave δ^{18} O record as well. We contend that this shared variance represents a common, summer monsoon forcing. A rigorous, independent, and quantitative test of this can be performed through analysis of the nonprimary (heterodyne) peaks within the cave δ^{18} O spectrum (Figure 5c) as follows.

[24] The orbital summer monsoon model indicates strengthened monsoons at both obliquity maxima and 125° into each precession cycle. If cave $\delta^{18}O$ shares this variance, then the spectra of the highly resolved and accurately dated cave $\delta^{18}O$ record must also contain the heterodyne tones of these two input frequencies. Mathematically, these tones can be isolated by crossing obliquity with Pmin_{lag8}. This pro-

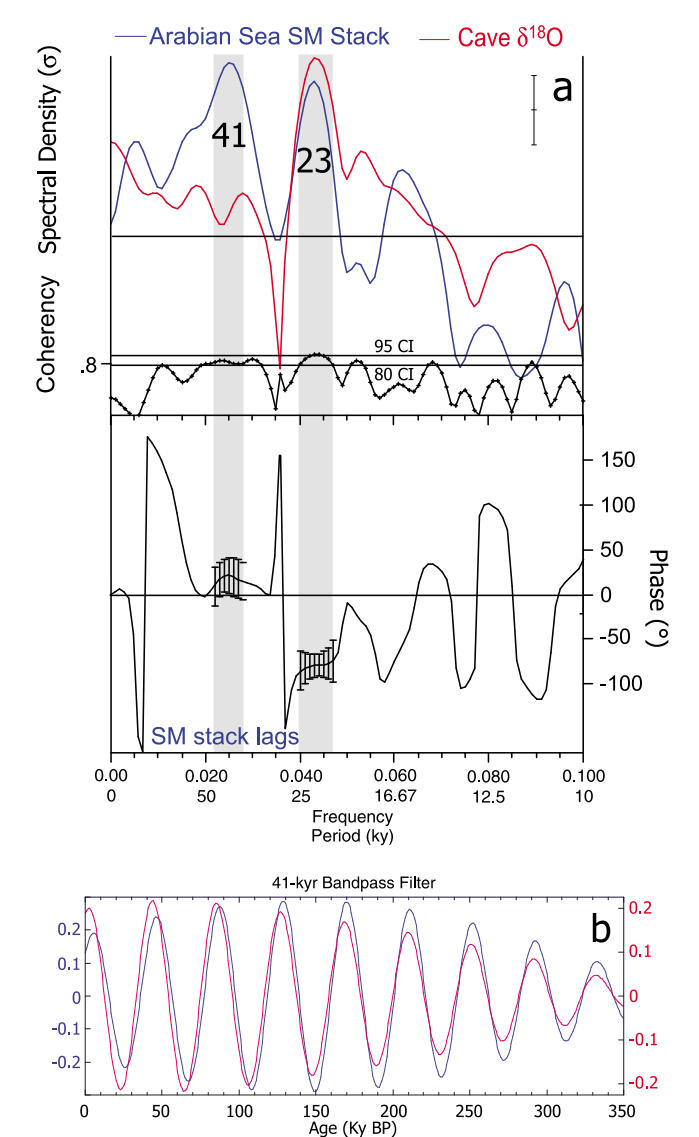


Figure 8. (a) Cross spectrum comparing the Arabian Sea summer monsoon stack [Clemens and Prell, 2003] to cave $\delta^{18}O$ [Cheng et al., 2009]. The SM stack is strongly coherent with cave $\delta^{18}O$ at the 23 kyr precession band. Coherence is indicated at the 41 kyr obliquity band as well, but the 41 kyr spectral peak in cave $\delta^{18}O$ is masked by the heterodyne peaks on either side. (b) The 41 kyr Gaussian band-pass filter of cave $\delta^{18}O$ and the Arabian Sea SM stack supporting the coherence and near-zero phase indicated in the cross spectral analysis (bandwidth is 0.024, central frequency is 0.024). Periods (1/frequency) of the main spectral peaks are labeled. Spectral densities are normalized and plotted on log scales. The horizontal lines indicate confidence at the 80% and 95% intervals for coherence.

duces a record with strong spectral peaks at 52.6 kyr and 14.7 kyr periods representing the beating between obliquity and precession ($1/41 \pm 1/23 = 1/14.7$ and 1/52.4) (Figure 9). The cross spectrum with cave δ^{18} O shows significant coherence and zero phase at these strong spectral peaks

documenting that cave $\delta^{18}O$ contains variance associated with a mechanism operating at the precession band (with a phase of -125°) and a mechanism operating at the obliquity band (with a phase of zero), as inferred from the Arabian Sea summer monsoon proxies. The cross products of obliquity and precession (with other phase lags) will also show strong coherence with the cave record, but not zero phase. The important point here is that the excellent chronology of the cave record allows discrimination among various cross product records on the basis of phase. This has not been previously possible given the more limited accuracy of marine and ice core chronologies. Having established that variance in the SM stack also resides within the cave $\delta^{18}O$ record, we next scale this variance to $\delta^{18}O$ units, subtract it from the cave record and analyze the residuals.

5. Removing the SM Component From Cave δ^{18} O and Analysis of Residuals

[25] The SM orbital model (section 3.3 and Figure 2d) is scaled to ‰ units by multiplying by the total variance in

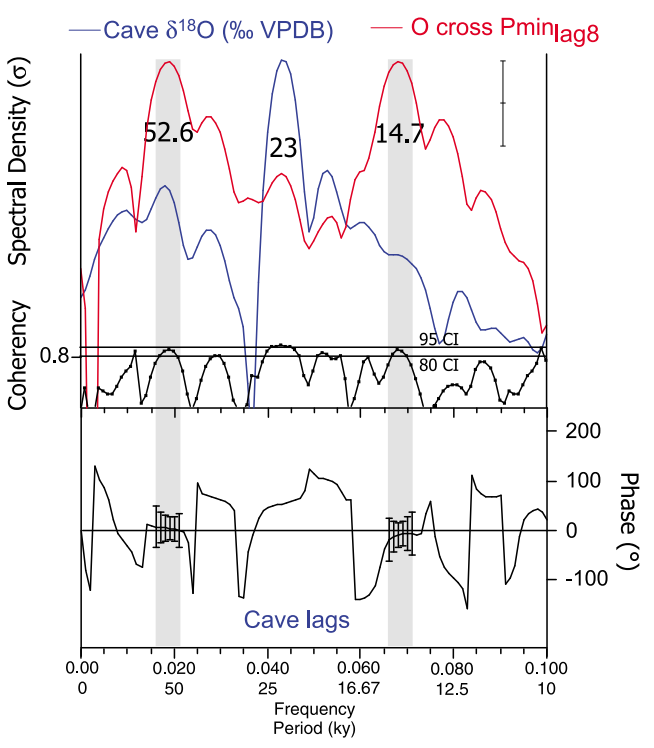


Figure 9. Cross spectrum comparing cave δ^{18} O to the cross product of obliquity and precession minima lagged by 125° (8 kyrs). Statistically significant coherence and zero phase at the dominant cross-product periods documents that summer monsoon variance at obliquity and precession, as depicted by the Arabian Sea stack, is also present in the cave δ^{18} O record. This is consistent with the strong coherence between cave δ^{18} O and the SM stack documented in Figure 8. Periods (1/frequency) of the main spectral peaks are labeled. Spectral densities are normalized and plotted on log scales. The horizontal lines indicate confidence at the 80% and 95% intervals for coherence.

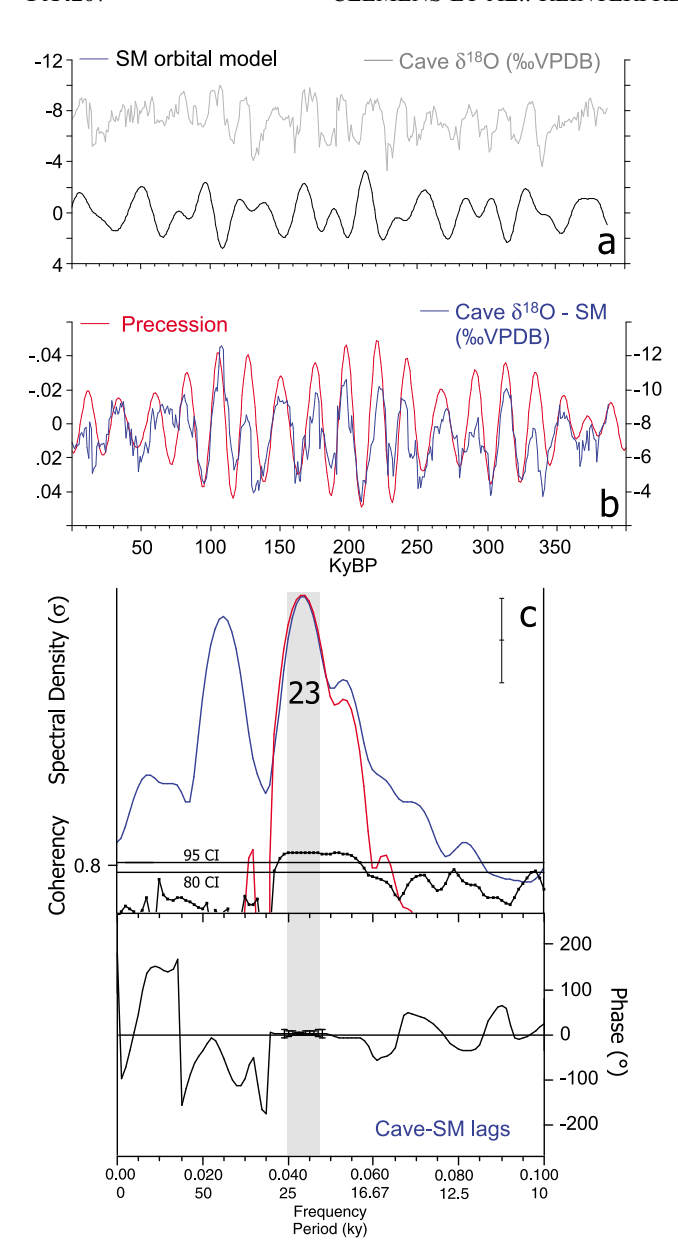


Figure 10. (a) Cave δ^{18} O and the Arabian Sea summer monsoon orbital model, (b) the residual after subtracting the SM orbital model from cave δ^{18} O and the cross spectrum comparing the residual with orbital precession. (c) The residual is highly coherent and in phase with precession minima, an orbital configuration characterized by the coldest northern hemisphere winters; the same result is found for cross spectra with minimum insolation at 30°N. The spectral peak at 41 kyr reflects the greater amount of obliquity variance in the Arabian Sea records relative to the cave record. Periods (1/frequency) of the main spectral peaks are labeled. Spectral densities are normalized and plotted on log scales. The horizontal lines indicate confidence at the 80% and 95% intervals for coherence.

cave δ^{18} O (Figure 10a). Subtracting this SM signal from the cave δ^{18} O signal yields a residual record that is very highly coherent and in phase (2.6 \pm 4°) with precession minima

(Figures 10b and 10c). Having subtracted what we interpret to be the SM signal, the question becomes, what is the interpretation of this residual cave signal that is so closely correlated to precession? We interpret this residual as the influence of the winter monsoon (temperature). We call on the changing temperature of winter atmospheric precipitation to drive the signal as follows.

[26] At the present orbital configuration (near precession maximum) the northern hemisphere experiences the warmest winters within the precession cycle. NH winters at precession minima are considerably colder. Analysis of FOAM results indicates a 5°C winter temperature range for southeastern Asia due only to changes in insolation forcing. This is consistent with orbital-scale winter season temperature changes of 6.5°C found in proxy data south of the cave sites, in the northern South China Sea [*Pflaumann and Jian*, 1999; *Wei et al.*, 2007]. In contrast, orbital-scale changes in summer season temperatures are only on the order of ~1°C [*Pflaumann and Jian*, 1999].

[27] Using a local (Nanjing and Wuhan) δ^{18} O precipitation versus temperature calibration for winter (DJF) [*IAEA*, 2008], a decrease in winter temperatures of 5°C would drive the modern DJF isotopic composition of rainfall from the current value of -6.2% to -9.6%. A similar change (-6.2% to -9.7%) is estimated using the global δ^{18} O_{ppt} versus temperature relationship [*Dansgaard*, 1964]. This winter temperature mechanism is supported by the strong correlation of cave δ^{18} O with absolute minimum insolation over the past 390 kyrs (Figure 11). The correlation between cave δ^{18} O and absolute minimum (winter) insolation is slightly stronger than the relationship between cave δ^{18} O and absolute maximum (summer) insolation.

[28] In summary, light cave δ^{18} O is produced by two different sources at two different times within the precession cycle. A light δ^{18} O response is produced via summer monsoon dynamics associated with the long transport path from the Indian ocean into Asia during summer [*Yuan et al.*, 2004]. Another light δ^{18} O response is produced by cooler winter season atmospheric precipitation at precession minima producing light δ^{18} O ppt. Thus, viable mechanisms exist for driving cave δ^{18} O toward light values via both summer and winter dynamics at the precession band; cave δ^{18} O responds to the combination of these two mechanisms.

6. A Cave δ^{18} O Orbital Model

[29] An orbital model for cave $\delta^{18}O$ may now be constructed as the sum of the summer monsoon (SM) and winter monsoon (WM) components of the precession band and the summer monsoon cross product (SMx) from section 4. The SM component consists of precession minima with a lag of -125° or 8 kyrs (Pmin_{lag8}). The WM component is composed of precession minima with no lag (Pmin). The SMx component is composed of obliquity crossed with lagged precession. The relative weighting of these three factors is derived from the ratio of spectral densities such that the orbital cave model is 0.4SM + 0.5WM + 0.1SMx as shown in Figure 12c. This model, incorporating both SM and WM dynamics, fits the cave $\delta^{18}O$ data better than maximum summer insolation forcing at 30°N. At the 23 kyr

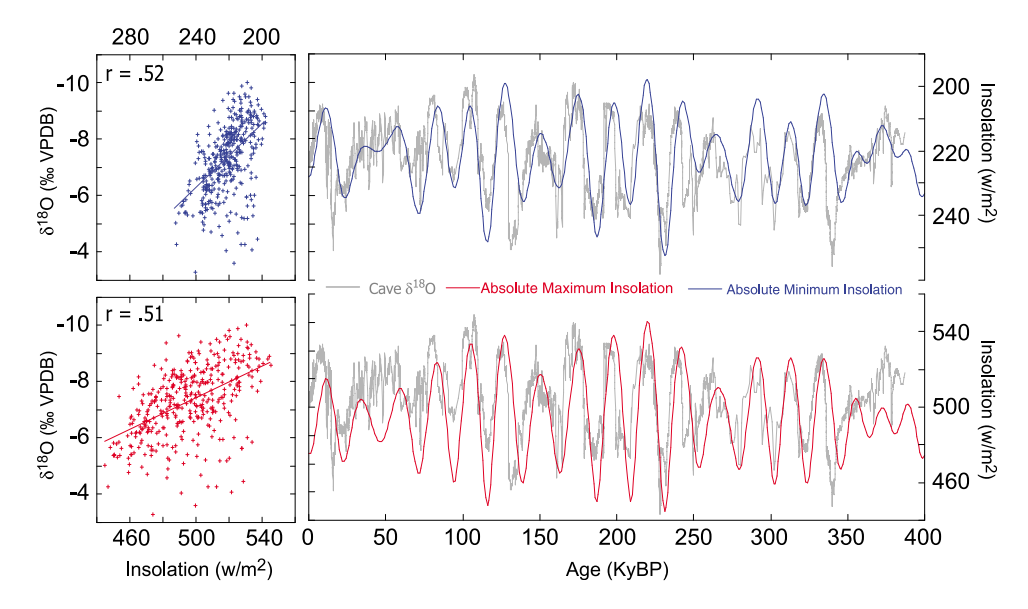


Figure 11. Time series and regressions indicating that cave δ^{18} O is equally well correlated to 30°N absolute minimum insolation and absolute maximum insolation. This is consistent with our interpretation of cave δ^{18} O as recording the combined influence of summer and winter dynamics.

band, coherence is exceptionally high and phase is $7 \pm 3^{\circ}$ as opposed to $45 \pm 3^{\circ}$ relative to maximum insolation forcing (Figures 12b and 12d). At the heterodyne bands (52.6 and 14.7 kyrs), coherence is significant and phase is zero ($-12 \pm 15^{\circ}$ and $-10 \pm 17^{\circ}$, respectively). In contrast, 30°N maximum insolation does not have variance at these heterodyne frequencies. Examining the time series in more detail (Figures 12a and 12b) it is clear that neither model works particularly well during periods of low eccentricity (20 to 70 ka and 350 to 390 ka). Cave δ^{18} O during these two intervals is better matched to the absolute minimum insolation record (Figure 11). This implies that the relative weightings applied above to the three-component model likely change over time.

[30] In summary, the cave δ^{18} O orbital model accounts for variance in the dominant primary spectral peak (23 kyrs) and the dominant nonprimary (heterodyne) peaks (52.6 and 14.7) as the result of both summer and winter dynamics. In section 7, we show that this interpretation of the cave δ^{18} O record is consistent with observed modern summer and winter rainfall amounts and isotopic composition as recorded in World Meteorological Organization (WMO), Global Network for Isotopes of Precipitation (GNIP) and National Center for Atmospheric Research (NCAR)/National Centers for Environmental Prediction (NCEP) data.

7. Modern Southeastern China Rainfall and Isotopic Composition

[31] The GNIP database [*IAEA*, 2008] provides insight into the seasonality of regional precipitation isotopic composition ($\delta^{18}O_{ppt}$) and precipitation amounts in the cave regions. The Nanjing GNIP site is proximal to Hulu cave while the Wuhan site is proximal to Sanbao and Linzhu caves (Figure 1 and Table 1). $\delta^{18}O_{ppt}$ indicates three distinct

isotopic sources and associated precipitation regimes. June, July, and August (JJA) are delineated as the primary summer monsoon months with an average $\delta^{18}O_{ppt}$ of $-8.78 \pm$ 1.22 ‰ and 192 mm precipitation per month, representing 48% of the annual precipitation. Rainfall in April and May (AM) has a distinctly different isotopic composition with an average $\delta^{18}O_{ppt}$ of -3.14 ± 0.98 % and 111 mm precipitation per month, representing 18% of the annual precipitation. Finally, September through March (SONDJFM) reflect another distinct source with an average $\delta^{18}O_{ppt}$ of $-6.60 \pm$ 1.16 % and 58 mm precipitation per month, representing 34% of total annual precipitation. These GNIP precipitation amount data are consistent with the much longer-term GHCNV2 World Meteorological Organization (WMO) station data most proximal to Hulu (station 58238) and Sanbao – Linzhu (station 57461), each reporting over 100 years of monthly average data (Table 1). Finally, these local WMO station and GNIP precipitation data are fully consistent with regional data averaged over all of southeast China (21° to 35°N, 106° to 122° E) on the basis of station data spanning 1951-1980 and with EAR-40 reanalysis data [Uppala et al., 2005] spanning 1957 to 2002 (Table 1).

[32] The critical point is that both regional and local data yield the same result, JJA precipitation accounts for less than 50% of the annual precipitation, contrasting sharply with the 80% previously reported based on the inclusion of May, September, and/or October as summer monsoon months [Dykoski et al., 2005; Kelly et al., 2006; Wang et al., 2001, 2008]. Including these months mixes different δ^{18} Oppt signals from distinctly different regimes, an assertion further supported by analysis of seasonal winds.

[33] NCEP/NCAR reanalysis data [Kalnay et al., 1996] indicate three distinct wind regimes (moisture sources) associated with the three distinct precipitation and $\delta^{18}O_{ppt}$ regimes. Winds during JJA are associated with southerly

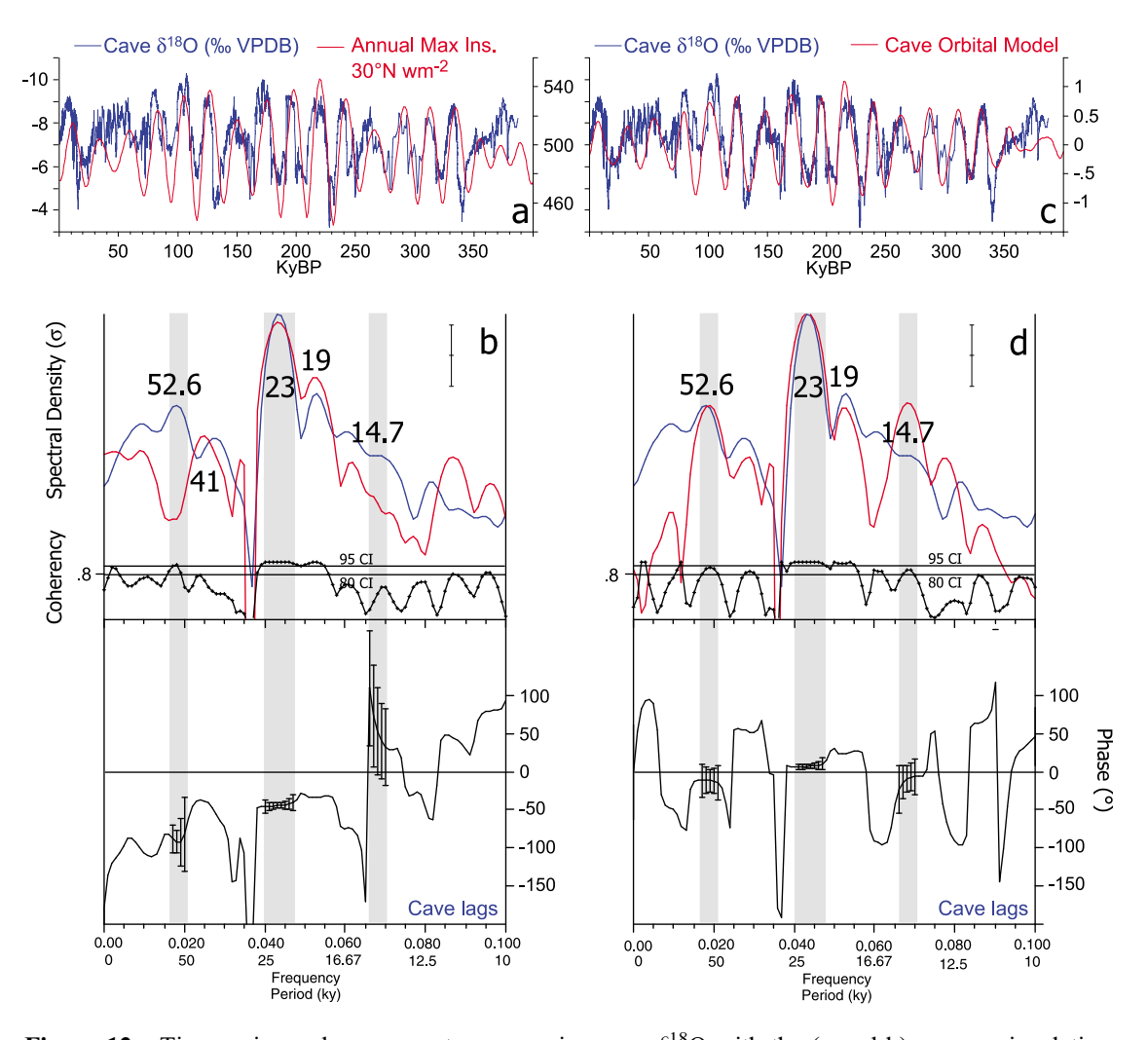


Figure 12. Time series and cross spectra comparing cave $\delta^{18}O$ with the (a and b) summer insolation forcing model and (c and d) the cave orbital model which includes summer monsoon variance derived from Arabian Sea summer monsoon proxies, winter temperature change, and the summer monsoon cross product. The cave orbital model fits the cave $\delta^{18}O$ data better in terms of the spectrum and phase at the primary and heterodyne frequencies. Periods (1/frequency) of the main spectral peaks are labeled. Spectral densities are normalized and plotted on log scales. The horizontal lines indicate confidence at the 80% and 95% intervals for coherence.

summer monsoon flow off the South China Sea (Figures 13a and 14b). The dominant source of this moisture is the SH Indian Ocean (Figures 3 and 4). The fall and winter months, SONDJFM, are associated with wind and moisture flow from the north, out of the continental interior (Figures 13b and 14c). Spring months, AM, are associated with easterly winds and moisture flow off the Pacific (Figures 13c and 14d), driven by circulation about the Pacific subtropical high [Simmonds et al., 1999].

[34] These modern isotopic precipitation sources span the observed range of cave $\delta^{18}O$ over the past 390 kyrs (Figure 14a). For the most part, the range of the summer and fall/winter $\delta^{18}O_{ppt}$ compositions can account for the full range of cave $\delta^{18}O$. On this basis, we contend that fall/winter sources are likely important in driving paleo cave $\delta^{18}O$ as well, especially given that the summer monsoon amount

effect is insufficient [Cheng et al., 2009; Johnson and Ingram, 2004; Maher, 2008; Wang et al., 2001]. Based on the modern GNIP data for the Nanjing and Wuhan average (Table 1 and Figure 14), a weighted budget predicts a modern cave δ^{18} O of -6.97%, after converting δ^{18} Oppt on the SMOW scale to calcite on the VPDB scale using the modern Hulu cave temperature of 15.4° C:

Cave
$$\delta^{18}O_{60}^{\text{V}}(\text{VPDB}) = (.48)(-8.73\%_0) + (.34)(-6.55\%_0) + (.18)(-3.09\%_0) = -6.97\%_0$$
 (1)

The predicted -6.97% value is consistent with the youngest Dongge cave calcite (DA, -7.18% at 0.1mm) ~ 1000 km to the southwest [Wang et al., 2005] and with the late Holocene values from the cave composite (Figure 14a). This

Table 1. Local and Regional $\delta^{18}O_{ppt}$ and Precipitation Data for Sites Proximal to Hulu and Sanbao Caves as Well as Southeast China Region^a

Month	Nanjing GNIP Precipitation (mm/month)	Wuhan GNIP Precipitation (mm/month)	Nanjing GNIP δ^{18} O (‰ VSMOW)	Wuhan GNIP δ ¹⁸ O (‰ VSMOW)	WMO Station 58238 GHCNV2 Precipitation From 1886 to 1991 (mm/month)	WMO Station 57461 GHCNV2 Precipitation From 1882 to 2008 (mm/month)	Southeast China EAR-40 Precipitation for 21°N-35°N 106°E-122°E From 1957 to 2002 (mm/day)	Southeast China Station Precipitation for 21°N–35°N 106°E–122°E From 1951 to 1980 (mm/month)
September	86	63	-7.99	-7.30	88.4	111.5	4.4	121.7
October	30	62	-6.66	-6.86	49.0	78.2	2.6	70.0
November	72	56	-7.18	-7.24	45.9	33.4	1.7	48.8
December	29	30	-8.06	-5.07	30.4	11.5	1.1	32.4
January	32	55	-7.89	-5.91	36.8	21.4	1.3	36.1
February	76	40	-5.97	-4.33	48.0	32.2	2.1	53.4
March	97	89	-6.75	-5.19	70.1	55.9	3.3	84.1
April	68	142	-2.91	-2.16	90.8	99.7	4.8	131.0
May	99	134	-4.49	-3.01	93.1	130.7	6.1	182.7
June	179	196	-9.55	-7.14	155.8	156.5	7.3	207.9
July	250	275	-9.88	-9.63	182.7	215.1	6.4	177.4
August Weighted	197	52	-9.13	-7.35	117.7	184.5	6.3	170.3
annual mean			-8.15	-7.04				

						Southeast	
				WMO		China EAR-40	
				Station 58238		Average	Southeast China
	Nanjing,		Nanjing,	GHCNV2	WMO Station	Precipitation	Average Station
	Wuhan	Nanjing,	Wuhan	Average	57461 GHCNV2	for 21°N-35°N	Precipitation for
	Average	Wuhan	Average	Precipitation	Average	106°E–122°E	21°N-35°N
	Precipitation	Average	GNIP δ^{18} O	From 1886 to	Precipitation	From	106°E-122°E
Season	(%)	Precipitation	(% VSMOW)	1991	From 1882 to 2008	1957 to 2002	From 1951 to 1980
SONDJFM	33.9%	58.4	-6.60 ± 1.16	36.5%	30.4%	34.7%	33.9%
AM	18.4%	110.8	-3.14 ± 0.98	18.2%	20.4%	23.1%	23.8%
JJA	47.7%	191.5	-8.78 ± 1.22	45.2%	49.2%	42.2%	42.2%
JJAS	53.9%			54.0%	59.1%	51.5%	51.5%

^aGNIP, http://nds121.iaea.org/wiser/; GHCNV2, http://www.ncdc.noaa.gov/oa/climate/research/ghcn/ghcngrid.html, http://climexp.knmi.nl/; EAR-40, http://climexp.knmi.nl/; Station, http://www.webgis-china.de/website/china_climate/viewer.htm.

budget is an accurate model for modern cave δ^{18} O, confirming that cave calcite records the weighted isotopic composition of annual average rainfall. We contend that seasonality is important in the past as well.

[35] The combination of GNIP, WMO, and NCAR/NCEP data present a clear and consistent picture; southeastern China is influenced by three distinct wind regimes linked to three distinct precipitation regimes, each with clearly defined $\delta^{18}{\rm O}_{\rm ppt}$ compositions; summer monsoon precipitation (JJA) accounts for less than half the signal. These modern data strongly support our reinterpretation of cave $\delta^{18}{\rm O}$ in the context of both summer and winter forcing. The -45° precession band phase of light cave $\delta^{18}{\rm O}$ reflects the input of a light SM component with a phase of 0° .

8. Summary

[36] A multiproxy set of marine and terrestrial data indicate that strong summer monsoons occur at obliquity (O) maxima and 125° (8 kyrs) after precession minima (Pmin_{lag8}). A summer monsoon orbital model is constructed as the sum of these two orbital parameters (O+Pmin_{lag8}). Cross spectral analysis demonstrates that variance contained in this orbital

model and in the Arabian Sea summer monsoon stack is also contained within the southeast China cave δ^{18} O record. We verify this by cross-spectral comparison of cave δ^{18} O with the cross product of obliquity and Pmin_{lag8}. Results indicate high coherence and zero phase at the predicted heterodyne frequencies. To our knowledge, this type of confirmation has never before been accomplished using both the coherence and phase of heterodynes and is only possible due to the accuracy of the cave chronology [Edwards et al., 1987]. Subtracting the summer monsoon orbital model from the cave δ^{18} O record yields a residual that is very highly coherent and in phase with precession minima and with absolute minimum winter insolation. This indicates that light cave δ^{18} O values are strongly influenced by changes in surface air temperatures at the orbital time scale. Both the regional and global $\delta^{18}{\rm O}_{\rm ppt}$ versus air temperature relationships confirm the sensitivity of southeastern China δ^{18} O_{ppt} to changing winter temperatures. [37] The primary finding of this work is that the timing of

[37] The primary finding of this work is that the timing of light cave δ^{18} O peaks should not be interpreted as reflecting the timing of strong summer monsoons alone; they reflect the combined influence of both summer monsoon circulation with a phase lag of 125° (8 kyrs) relative to precession minima and winter temperature changes with a phase of 0°

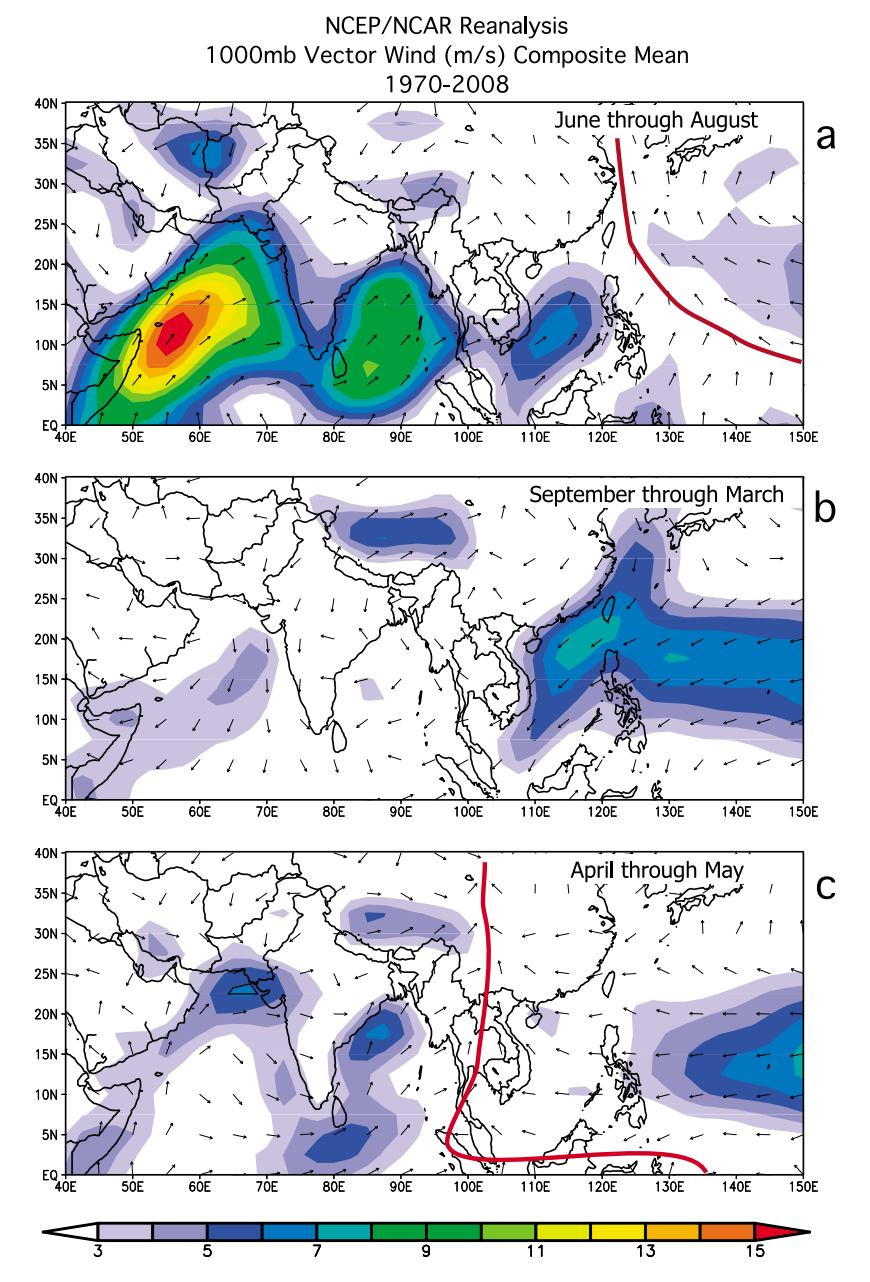


Figure 13. NCEP/NCAR 1000 mb composite mean vector winds (1970–2008) for (a) June, July, and August, (b) September through March, and (c) April through May. These three wind regimes are associated with distinct $\delta^{18}O_{ppt}$ values in the GNIP data reflecting a Pacific source (AM, -3.1 ‰), an Indian Ocean source, via the South China Sea (JJA, -8.8 ‰) and a continental source (SONDJFM, -6.6 ‰). The red lines on the JJA and AM maps depict the convergence between winds sourced from the North Pacific subtropical high and those from the Indian Ocean and South China Sea. Maps provided by the NOAA/ESRL Physical Sciences Division, Boulder Colorado: <www.cdc.noaa.gov/>.

relative to precession minima. This is strongly supported by the coherence and phase analysis of heterodynes in the cave $\delta^{18}{\rm O}$ spectrum. Analysis of Global Network for Isotopes of Precipitation (GNIP) data and World Meteorological Organization (WMO) data demonstrate that the most recent cave $\delta^{18}{\rm O}$ calcite reflects the combined summer and winter $\delta^{18}{\rm O}_{\rm ppt}$ signals, strongly supporting our interpretation that

the timing of light cave $\delta^{18}O$ should not be interpreted as reflecting the timing of strong summer monsoons alone.

Appendix A

A1. Multiproxy Synthesis

[38] A synthesis of publications spanning the past two decades yields 19 proxy records interpreted to reflect aspects

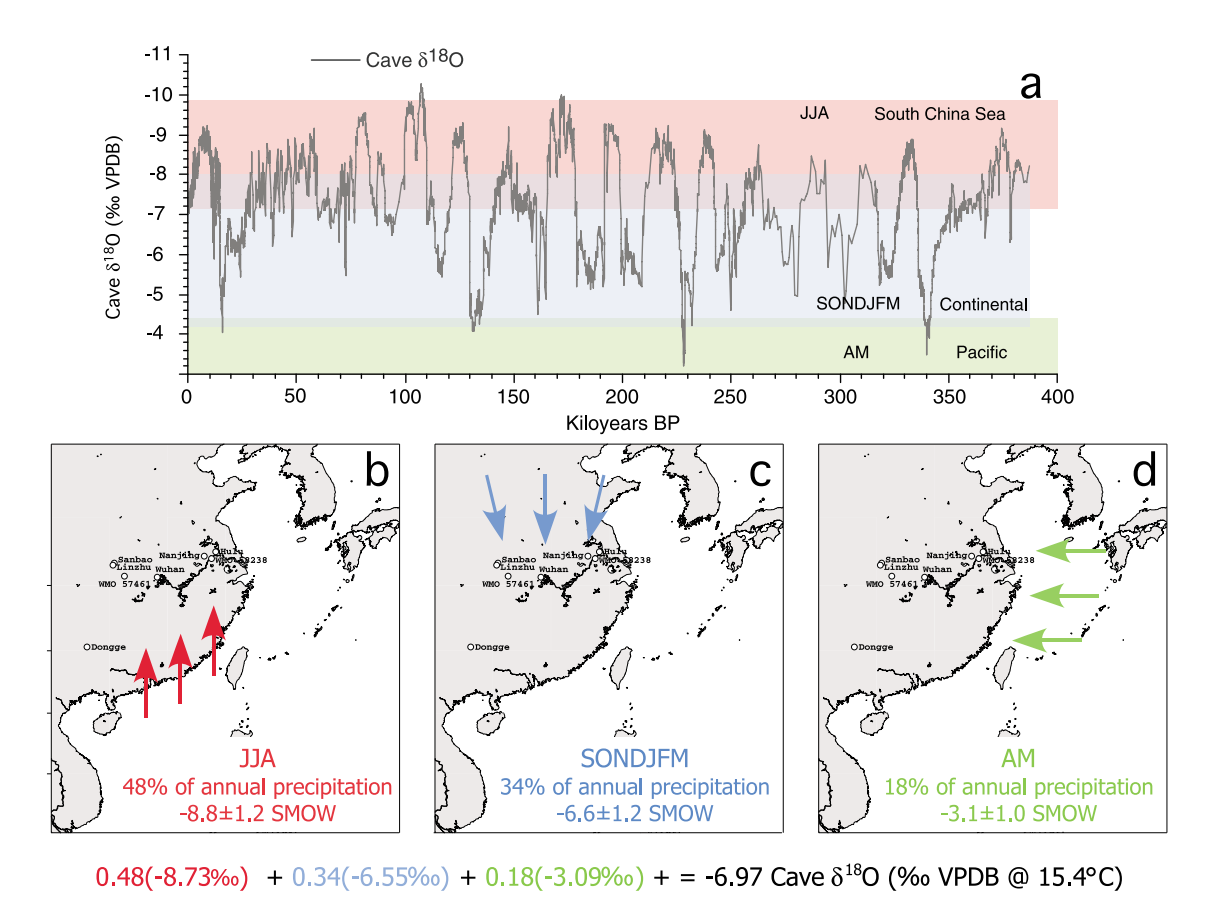


Figure 14. Cave δ^{18} O and modern seasonality of precipitation amount, δ^{18} O_{ppt}, and wind direction. The range of δ^{18} O_{ppt} during the summer, fall/winter, and spring span the range of cave δ^{18} O over the past 390 kyrs. The weighted annual average of all three seasons accurately predicts the value of modern cave calcite indicating that cave calcite reflects weighted annual average isotopic composition of rainfall, including both winter and summer seasons. For Figure 14a the δ^{18} O_{ppt} ranges on the SMOW scale have been converted to calcite on the VPDB scale at Hulu cave temperatures of 15.4°C.

of Late Pleistocene summer monsoon circulation from the Indian and East Asian monsoon systems (Table A1 and Figures 1 and A1). Three of these records have radiometric chronologies; all others are tied directly to the benthic marine (SPECMAP) chronology. Proxy phases are reported relative to precession minima (21 June perihelion) reflecting the strongest northern hemisphere summer insolation maxima [Berger, 1978; Clemens and Prell, 2007; Laskar et al., 1993]. Proxy phase was calculated by cross spectral analysis [Jenkins and Watts, 1968] relative to orbital precession for the three records with radiometric chronologies. The phases of the remaining proxies were calculated relative to the paired δ^{18} O from the same samples or relative to the proxy used in tuning to the marine chronology. The phase relative to precession minima was then established by assigning δ^{18} O minima a value of -78° [Imbrie et al., 1984; Lisiecki and Raymo, 2005]. This approach eliminates age model differences associated with the subjective nature of correlating structure within records.

[39] Eighteen of the nineteen records cluster about a phase of $-125 \pm 17^{\circ}$. This is an exceptionally tight clustering considering the large geographic region and diverse array of

summer monsoon proxies under consideration. Cave $\delta^{18}O$ exhibits a phase of -45° , clearly an outlier in this context. The 18 records that cluster include both high- and low-resolution records from land and ocean archives. Six records have centennial-scale temporal resolution (e.g., Figures 2b, 2c, and 2e), eleven have resolutions of \sim 3 kyrs or less (e.g., Figures 2c–2e) and one, a resolution of \sim 5 kyrs. The phase distribution indicates no relationship between temporal resolution and phase indicating that aliasing is not an issue, consistent with the fact that all exceed the Nyquist resolution necessary to confidently estimate phase relative to a 23 kyr cycle. Similarly, the phase distribution indicates no systematic differences relative to proxies from the Indian and East Asian monsoon subsystems, or relative to those from terrestrial and marine environments.

[40] The 18 records that cluster represent a broad array of proxies monitoring diverse, independent aspects of summer monsoon circulation using a variety of chemical, physical, faunal, and isotopic proxies. These proxies include wind-driven upwelling-induced productivity in the Arabian Sea [Clemens et al., 1991; Clemens and Prell, 2003; Leuschner and Sirocko, 2003; Reichart et al., 1998; Schmiedl and

Table A1. Phase of Indian and East Asian Summer Monsoon Proxies Relative to Precession Minima^a

Chen et al. [2003]South China SeaSSTSchmiedl and Leuschner [2005]Arabian Sea% G. bulloidesSchmiedl and Leuschner [2005]Arabian SeaBa/AlLeuschner and Sirocko [2003]Arabian SeaBa/AlReichart et al. [1998]Arabian SeaBa/AlReichart et al. [1998]Arabian SeaBa/AlReichart et al. [1998]Arabian SeaBa/AlReichart et al. [1998]Arabian Sea% G. bulloidesMorley and Heusser [1997]Philipine Sea% CryptomeriaIgarashi and Oba [2006]NW PacificjaponicaClemens et al. [1991];Arabian Seagrain sizeClemens and Prell [2003]Arabian SeaBiogenic Ba fluxClemens et al. [1991];Arabian Sea% G. bulloidesClemens et al. [1991];Arabian SeaBiogenic opal fluxClemens et al. [1991];Arabian Sea% G. bulloidesClemens et al. [1991];Arabian SeaBiogenic opal fluxClemens et al. [1991];Arabian SeaBiogenic opal fluxClemens et al. [1991];Arabian SeaPiotal NitrogenClemens et al. [1991];Arabian SeaBiogenic opal fluxClemens et al. [1991];Arabian SeaBiogenic opal fluxClemens and Prell [2003]Arabian SeaTotal NitrogenIndependent and Inouchi [2007]Lake Biwa, JapanTotal NitrogenClemens and Inouchi [2007]Lake Biwa, JapanTotal CarbonClemens and Prell [2008]Arabian SeaPiotal Carbon	Wind-driven Convergence Productivity Hoides (upwelling) Productivity (upwelling) N (upwelling) N OMZ denitrification Al Productivity (upwelling) Hoides Productivity (upwelling) Hoides Productivity (upwelling)		X 0 444	δ ¹⁸ O planktonic δ ¹⁸ O benthic tephra tephra 14C, δ ¹⁸ O planktonic, tephra 14C, δ ¹⁸ O planktonic 14C, δ ¹⁸ O planktonic 14C, δ ¹⁸ O planktonic	-117 ± 67 -103 ± 9 -122 ± 49 -112 ± 91	-128 ± 25
Arabian Sea % G. b. Arabian Sea Arabian Sea Arabian Sea Ba Arabian Sea Ba Arabian Sea % G. b. Philipine Sea % Cryp NW Pacific Jipo Arabian Sea grain Arabian Sea Biogenic Arabian Sea Biogenic Arabian Sea Biogenic Lake Biwa, Japan Total N Manana Arabian Sea Biogenic				δ^{18} O benthic ϵ^{18} C, δ^{18} O planktonic, tephra 14 C, δ^{18} O planktonic 14 C, δ^{18} O planktonic 14 C, δ^{18} O planktonic	-117 ± 67 -103 ± 9 -122 ± 49 -112 ± 91	
Arabian Sea Arabian Sea Arabian Sea Arabian Sea Ba Arabian Sea % G. b. % Cryp Philipine Sea % Cryp NW Pacific Litho Arabian Sea Biogenic Arabian Sea Biogenic Lake Biwa, Japan Total N Lake Biwa, Japan Total N Lake Biwa, Japan Total N South China Sea Biogenic South China Sea Biogenic South China Sea Biogenic South China Sea Biogenic Marabian Sea Biogenic Lake Biwa, Japan Total N Marabian Sea Biogenic Casta				tephra 14C, δ^{18} O planktonic 14C, δ^{18} O planktonic 14C, δ^{18} O planktonic	-103 ± 9 -122 ± 49 -112 ± 91	
Arabian Sea Barabian Sea Arabian Sea Barabian Sea % Cryp Philipine Sea % Cryp NW Pacific japo Arabian Sea grain Litho Arabian Sea grain Arabian Sea grain Arabian Sea Biogenic Jake Biwa, Japan Total N South China Sea Biogenic South China Sea Biogenic Macana				14 C, 618 O planktonic 14 C, 618 O planktonic	-112 ± 91	
Arabian Sea % G. b Philipine Sea % Cryp NW Pacific japo Jidoo Arabian Sea grain Arabian Sea Biogenic Arabian Sea Biogenic Arabian Sea Biogenic Lake Biwa, Japan Total N South China Sea Biogenic Magenic		•		¹⁴ C, δ^{18} O planktonic	145 - 21	
Philipine Sea japo NW Pacific , japo NW Pacific , japo Litho Litho Arabian Sea grain Arabian Sea Biogenic Arabian Sea Biogenic Arabian Sea Biogenic Lake Biwa, Japan Total N Lake Biwa, Japan Total N South China Sea Biogenic Maganic					-145 ± 31	
NW Pacific japon Litho Litho Litho Arabian Sea grain Arabian Sea Biogenic Arabian Sea % G. b. Arabian Sea Biogenic Arabian Sea Biogenic Arabian Sea Biogenic Arabian Sea Biogenic South China Sea Biogenic Arabian Sea Biogenic	omeria	350 2.0	RC1499	C. davisiana δ^{18} O benthic, 14 C,		-136 ± 11
rell [2003] Arabian Sea grain 991]; Arabian Sea Biogenic rell [2003] Arabian Sea % G. b. 991]; Arabian Sea % G. b. rell [2003] Arabian Sea Biogenic reli [2003] Lake Biwa, Japan Total N. rchi [2007] Lake Biwa, Japan Total Sea South China Sea Biogenic Mosenic Mosenic	ica Precipitation enic	144 0.6	MD012421	tephra		-151 ± 24
Arabian Sea Biogenic	size Wind strength	350 3.2	RC2761	δ^{18} O benthic	-144 ± 12	
Arabian Sea		350 2.5	722	δ^{18} O benthic	-100 ± 10	
red! [2003] Arabian Sea Biogenic red! [2007] Lake Biwa, Japan Total N roti! [2007] Lake Biwa, Japan Total N South China Sea Biogenic 008]		350 3.2	RC2761	δ^{18} O benthic	-117 ± 21	
con [2007] Lake Biwa, Japan con [2007] Lake Biwa, Japan 008] South China Sea	×		•	δ^{18} O benthic	-109 ± 21	
No8] South China Sea	trogen 290 arbon 290	290 0.15 290 0.15	Takashima-oki Takashima-oki	C, tephra		$-123 \pm 1/$ -147 ± 23
	Ba flux Productivity (runoff)			δ ¹⁸ O benthic		-130 ± 13
[2008] Loess Plateau su	euc bility Soil formation OM7	500 2.0	Znaojiacnuan-Lingiai stack	to δ^{18} O max		-94 ± 11
Attabet et al. [1995] Arabian Sea δ^{15} N South China Sea Ba/Al	deni	430 3.2 150 0.5		δ^{18} O benthic	-137 ± 20	-144 ± 16
Cheng et al. [2009] Southeastern China Speleothem δ^{18} O	m δ^{18} O Precipitation	390 0.09	Linzhu composite	$^{230}{ m Th}$		-45 ± 4

 ^{a}P min. 21 June perihelion, $\omega=90^{\circ}.$

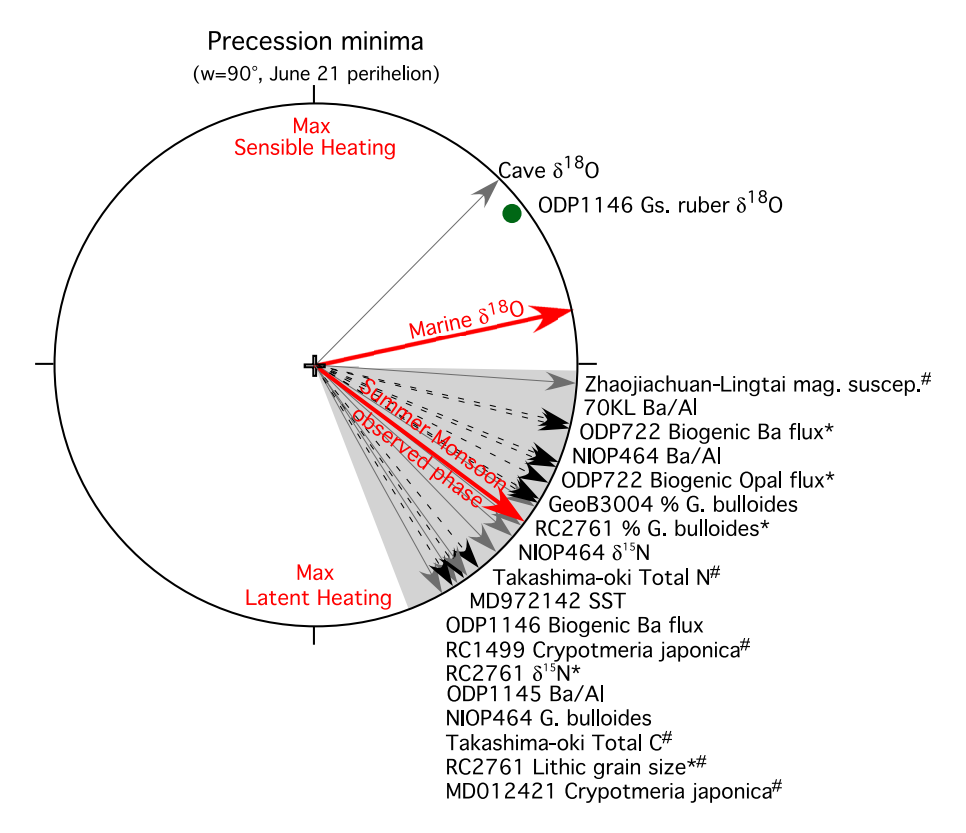


Figure A1. Precession band phase wheel indicating the timing of Indo-Asian summer monsoon proxies from marine and terrestrial records. Phase wheel construct is as described in the Figure 5 caption. The timing of potential summer monsoon (SM) forcing mechanisms are denoted by red text within the phase wheel including maximum sensible heating over Asia in summer (0°) [Prell and Kutzbach, 1992], ice volume minima (-78°) [Prell and Kutzbach, 1992], and maximum export of latent heat from the southern subtropical Indian Ocean (-180°) [Clemens and Prell, 2003; Liu et al., 2006]. Black dashed vectors indicate the phase of Indian summer monsoon proxy maxima, while gray vectors indicate the phase of East Asian summer monsoon proxy maxima. Cave δ^{18} O is a clear outlier relative to all other Indian and East Asian summer monsoon proxies. However, within error, cave δ^{18} O is in phase with site 1146 surface water δ^{18} O (green dot), a proxy forced by a broad range of summer, winter, glacial, and interglacial dynamics. Grey shading indicates 2σ standard deviation of the mean phase (red vector) of the 18 summer monsoon proxies that cluster about -125° . Pound sign indicates proxies that reflect terrestrial summer monsoon processes. Asterisk indicates proxies used in the Arabian Sea summer monsoon stack shown in Figure 2d.

Leuschner, 2005], denitrification in the Arabian Sea oxygen minimum zone [Altabet et al., 1995; Reichart et al., 1998], the transport capacity of winds circulating about the Asian low [Clemens et al., 1991; Clemens, 1998], soil formation on the Chinese Loess Plateau [Clemens et al., 2008; Sun et al., 2006], rainfall in southeast Japan [Igarashi and Oba, 2006; Iwamoto and Inouchi, 2007; Morley and Heusser, 1997], runoff-induced productivity in the south China Sea [Clemens et al., 2008; Sun et al., 2008], and wind-induced convergent sea surface temperatures in the South China Sea [Chen et al., 2003]. We interpret the tight phase coupling of these eighteen proxies as evidence that they are all responding to the one climate mechanism they all share in common, summer monsoon circulation. The likelihood is extraordinarily small that all 18 of these chemical, physical, faunal, and isotopic proxies from this wide array of marine

and terrestrial environments are systematically biased by the same nonmonsoon mechanism, yielding an incorrect phase. Thus, we interpret the precession band phase of the summer monsoon to be -125° , not -45° as suggested by cave δ^{18} O.

A2. Cross Spectral Methods

[41] Our Blackman-Tukey cross-spectral analyses follow standard methods [Jenkins and Watts, 1968; Imbrie et al., 1989] using ARAND software available at http://www.ncdc.noaa.gov/paleo/softlib/, the results of which are displayed as spectral density, coherency and phase spectra spanning the 101 frequency bands ranging 0 to the Nyquist frequency. Spectral densities (variance/frequency) are normalized and plotted on a log scale. Coherency is a measure of the maximum linear correlation between two signals

when the phase is set to zero, with values ranging from 0 to 1; Coherence squared represents the fraction of variance in one signal that is linearly related to variance in the other. Values of significance are assessed at the 80% and 95% fiducial levels. Phase estimates span 0 to 360° and can be directly converted to time for specific frequency band. For example, a phase lag of 90° at the precession band indicates a lag of 90°/360° \times 23,000 years = 5750 years. This approach requires that time series be interpolated to a constant time interval. For cross spectra in the main body of the paper the interpolated value was 1 kyr when crossing the cave δ^{18} O record with insolation or orbital data and 2 kyrs when crossing any record with the Arabian Sea SM stack. Both the cave and Arabian Sea records are of sufficient temporal resolution and of sufficient length to resolve the

variance and phase in the frequency bands of interest. Interpolation varied for cross-spectral analysis of records in Table A1 (Appendix A) according to the resolution of the various records, with interpolated intervals ranging from 1 to 5 kyrs. Both the Blackman-Tukey method and higher-resolution approaches such as the multitaper method [*Thomson*, 1982] yield similar results for orbital periods and associated heterodynes [*Imbrie et al.*, 1989; *Clemens and Tiedemann*, 1997].

[42] **Acknowledgments.** We thank Nick Pisias and two anonymous reviewers for constructive comments and criticism. This work was supported by U.S. National Science Foundation grants OCE0352215, OCE0082765, and OCE0352362 and National Basic Research Program of China grant 2010CB833403.

References

- Altabet, M. A., R. Francois, D. W. Murray, and W. L. Prell (1995), Climate-related variations in denitrification in the Arabian Sea from sediment ¹⁵N/¹⁴N ratios, *Nature*, *373*, 506–509, doi:10.1038/373506a0.
- Barnett, T. P., L. Dumenil, U. Schlese, E. Roeckner, and M. Latif (1989), The effect of Eurasian snow cover on regional and global climate variations, *J. Atmos. Sci.*, 46, 661–685.
- Berger, A. (1977), Long-term variations of the earth's orbital elements, *Celestial Mech.*, *15*, 53–74, doi:10.1007/BF01229048.
- Berger, A. L. (1978), Long-term variations of caloric insolation resulting from the Earth's orbital elements, *Quat. Res.*, *9*, 139–167, doi:10.1016/0033-5894(78)90064-9.
- Bosilovich, M. G., and S. D. Schubert (2002), Water vapor tracers as diagnostics of the regional hydrological cycle, *J. Hydrometeorol.*, 3, 149–165, doi:10.1175/1525-7541(2002) 003<0149:WVTADO>2.0.CO;2.
- Chen, M.-T., L.-J. Shiau, P.-S. Yu, T.-C. Chiu, Y.-G. Chen, and K.-Y. Wei (2003), 500,000year records of carbonate, organic carbon, and foraminiferal sea-surface temperature from the southeastern South China Sea (near Palawan Island), *Palaeogeogr. Palaeoclimatol. Palaeoecol.*, 197(1–2), 113–131, doi:10.1016/S0031-0182(03) 003804
- Cheng, H., R. L. Edwards, Y. J. Wan, X. G. Ko, Y. F. Ming, M. J. Kelly, X. F. Wang, C. D. Gallup, and W. G. Liu (2006), A penultimate glacial monsoon record from Hulu Cave and two-phase glacial terminations, *Geology*, 34 (3), 217–220, doi:10.1130/G22289.1.
- Cheng, H., R. L. Edwards, W. S. Broecker, G. H. Denton, X. G. Kong, Y. J. Wang, R. Zhang, and X. F. Wang (2009), Ice age terminations, *Science*, 326(5950), 248–252, doi:10.1126/science.1177840.
- Clemens, S. C. (1998), Dust response to seasonal atmospheric forcing: Proxy evaluation and calibration, *Paleoceanography*, *13*, 471–490, doi:10.1029/98PA02131.
- Clemens, S. C., and W. L. Prell (2003), A 350,000 year summer-monsoon multi-proxy stack from the Owen Ridge, Northern Arabian Sea, *Mar. Geol.*, 201(1–3), 35–51, doi:10.1016/S0025-3227(03)00207-X.
- Clemens, S. C., and W. L. Prell (2007), The timing of orbital-scale Indian monsoon changes, *Quat. Sci. Rev.*, 26, 275–278, doi:10.1016/j.quascirev.2006.11.010.
- Clemens, S. C., and R. Tiedemann (1997), Eccentricity forcing of Pliocene-Early Pleisto-

- cene climate revealed in a marine oxygen isotope record, *Nature*, 385, 801–804.
- Clemens, S. C., W. L. Prell, D. Murray, G. Shimmield, and G. Weedon (1991), Forcing mechanisms of the Indian Ocean monsoon, *Nature*, 353, 720–725, doi:10.1038/353720a0.
- Clemens, S., W. Prell, and Y. Sun (2008), Reconciling cave, marine, and loess proxies for summer monsoon strength at the precession band, *Eos Trans. AGU*, 89(53), Fall Meet. Suppl., Abstract PP24a-06.
- Dansgaard, W. (1964), Stable isotopes in precipitation, *Tellus*, *16*, 436–468, doi:10.1111/j.2153-3490.1964.tb00181.x.
- Ding, Y., and J. C. L. Chan (2005), The East Asian summer monsoon: An overview, *Meteorol. Atmos. Phys.*, 89, 117–142, doi:10.1007/s00703-005-0125-z.
- Ding, Y., C. Li, and Y. Liu (2004), Overview of the South China Sea monsoon experiment, *Adv. Atmos. Sci.*, 21, 343–360, doi:10.1007/BF02915563.
- Dykoski, C. A., R. L. Edwards, H. Cheng, D. Yuan, Y. Cai, M. Zhang, Y. Lin, J. Qing, Z. An, and J. Revenaugh (2005), A high-resolution, absolute-dated Holocene and deglacial Asian monsoon record from Dongge Cave, China, *Earth Planet. Sci. Lett.*, 233(1–2), 71–86, doi:10.1016/j.epsl.2005.01.036.
- Edwards, L. R., J. H. Chen, and G. J. Wasserburg (1987), ²³⁸U²³⁴U²³⁰Th²³²Th systematics and the precise measurement of time over the past 500,000 years, *Earth Planet. Sci. Lett.*, 81(2–3), 175–192.
- Emile-Geay, J., M. A. Cane, N. Naik, R. Seager, A. C. Clement, and A. van Geen (2003), Warren revisited: Atmospheric freshwater fluxes and "Why is no deep water formed in the North Pacific", *J. Geophys. Res.*, 108(C6), 3178, doi:10.1029/2001JC001058.
- Hastenrath, S., and L. Greischar (1993), The monsoonal heat-budget of the hydrosphere-atmosphere system in the Indian-Ocean sector, *J. Geophys. Res.*, *98*(C4), 6869–6881.
- Huybers, P. (2006), Early Pleistocene glacial cycles and the integrated summer insolation forcing, *Science*, 313(5786), 508–511, doi:10.1126/science.1125249.
- IAEA (2008), Global network of isotopes in precipitation, GNIP database, report, World Meteorol. Organ., Vienna.
- Igarashi, Y., and T. Oba (2006), Fluctuations in the East Asian monsoon over the last 144 ka in the northwest Pacific based on a high-resolution

- pollen analysis of IMAGES core MD01-2421, *Quat. Sci. Rev.*, 25(13–14), 1447–1459.
- Imbrie, J., J. D. Hays, D. G. Martinson, A. McIntyre, A. C. Mix, J. J. Morley, N. G. Pisias, W. L. Prell, and N. J. Shackleton (1984), The orbital theory of Pleistocene climate: Support from a revised chronology of the marine δ^{18} O record, in *Milankovitch and Climate: Understanding the Response to Astronomical Forcing*, edited by A. L. Berger et al., pp. 269–305, D. Reidel, Hingham, Mass.
- Imbrie, J., A. McIntyre, and A. Mix (1989), Oceanic response to orbital forcing in the late Quaternary: Observational and experimental strategies, in *Climate and Geosciences*, edited by A. Berger et al., pp. 121–164, Kluwer, Boston.
- Iwamoto, N., and Y. Inouchi (2007), Reconstruction of millennial-scale variations in the East Asian summer monsoon over the past 300 ka based on the total carbon content of sediment from Lake Biwa, Japan, *Environ. Geol.*, 52(8), 1607–1616.
- Jenkins, G. M., and D. G. Watts (1968), Spectral Analysis and its Applications, 525 pp., Holden Day, Oakland, Calif.
- Johnson, K. R., and B. L. Ingram (2004), Spatial and temporal variability in the stable isotope systematics of modern precipitation in China: Implications for paleoclimate reconstructions, *Earth Planet. Sci. Lett.*, 220(3–4), 365–377, doi:10.1016/S0012-821X(04)00036-6.
- Kalnay, E., et al. (1996), The NCEP/NCAR 40year reanalysis project, *Bull. Am. Meteorol. Soc.*, 77, 437–471, doi:10.1175/1520-0477 (1996)077<0437:TNYRP>2.0.CO;2.
- Kelly, M. J., R. L. Edwards, H. Cheng, D. X. Yuan, Y. J. Cai, M. L. Zhang, Y. S. Lin, and Z. S. An (2006), High resolution characterization of the Asian Monsoon between 146,000 and 99,000 years BP from Dongge Cave, China and global correlation of events surrounding Termination II, *Palaeogeogr. Palaeoclimatol. Palaeoecol.*, 236(1–2), 20–38, doi:10.1016/j.palaeo.2005.11.042.
- Kutzbach, J. E., X. Liu, Z. Liu, and G. Chen (2007), Simulation of the evolutionary response of global summer monsoons to orbital forcing over the last 280,000 years, *Clim. Dyn.*, 30, 567–579.
- Laskar, J., F. Jouzel, and F. Boudin (1993), Orbital, precessional, and insolation quantities for the Earth from -20 Myr to +10 Myr, *Astron. Astrophys.*, 270, 522-533.

- Leuschner, D. C., and F. Sirocko (2003), Orbital insolation forcing of the Indian Monsoon: A motor for global climate changes?, *Palaeogeogr. Palaeoclimatol. Palaeoecol.*, 197, 83–95.
- Lisiecki, L., and M. Raymo (2005), A Pliocene-Pleistocene stack of 57 globally distributed benthic δ^{18} O records, *Paleoceanography*, 20, PA1003, doi:10.1029/2004PA001071.
- Liu, T., and W. Tang (2004), Oceanic influence on the precipitation in India and China as observed by REMM and QuikSCAT, paper presented at The 2nd International Tropical Rainfall Measuring Mission Science Conference, Jpn. Aerosp. Explor. Agency, Tokyo.
- Liu, T., and W. Tang (2005), Estimating moisture transport over oceans using space-based observations, *J. Geophys. Res.*, 110, D10101, doi:10.1029/2004JD005300.
- Liu, T. W., A. Zhang, and J. K. B. Bishop (1994), Evaporation and solar irradiance as regulators of sea surface temperature in annual and interannual changes, *J. Geophys. Res.*, 99, 12,623–612,637.
- Liu, X., Z. Liu, J. E. Kutzbach, S. C. Clemens, and W. L. Prell (2006), Hemispheric insolation forcing of the Indian Ocean and Asian Monsoon: Local versus remote impacts, *J. Clim.*, 19, 6195–6208, doi:10.1175/JCLI3965.1.
- Loschnigg, J., and P. J. Webster (2000), A coupled ocean-atmosphere system of SST modulation for the Indian Ocean, *J. Clim.*, *13*(19), 3342–3360
- Maher, B. A. (2008), Holocene variability of the East Asian summer monsoon from Chinese cave records: A re-assessment, *Holocene*, 18(6), 861–866, doi:10.1177/0959683608095569.
- Morley, J. J., and L. E. Heusser (1997), Role of orbital forcing in East Asian monsoon climates during the last 350 kyr: Evidence from terrestrial and marine climate proxies from core RC14-99, *Paleoceanography*, 12, 483–494.
- Park, S. C., B. J. Sohn, and B. Wang (2007), Satellite assessment of divergent water vapor transport from NCEP, ERA40, and JRA25 reanalyses over the Asian summer monsoon region, *J. Meteorol. Soc. Jpn.*, 85, 615–632, doi:10.2151/jmsj.85.615.
- Pflaumann, U., and Z. Jian (1999), Modern distribution patterns of planktonic foraminifera in the South China Sea and western Pacific: A new transfer technique to estimate regional sea-surface temperatures, *Mar. Geol.*, *156*, 41–83, doi:10.1016/S0025-3227(98)00173-X.
- Prell, W. L., and J. E. Kutzbach (1987), Monsoon variability over the past 150,000 years, J. Geophys. Res., 92(D7), 8411–8425, doi:10.1029/JD092iD07p08411.

- Prell, W. L., and J. E. Kutzbach (1992), Sensitivity of the Indian monsoon to forcing parameters and implications for its evolution, *Nature*, *360*, 647–652, doi:10.1038/360647a0.
- Reichart, G. J., L. J. Lourens, and W. J. Zachariasse (1998), Temporal variability in the northern Arabian Sea oxygen minimum zone (OMZ) during the last 225,000 years, *Paleoceanography*, 13, 607–621, doi:10.1029/98PA02203.
- Rohling, E. J., Q. S. Liu, A. P. Roberts, J. D. Stanford, S. O. Rasmussen, P. L. Langen, and M. Siddall (2009), Controls on the East Asian monsoon during the last glacial cycle, based on comparison between Hulu Cave and polar ice-core records, *Quat. Sci. Rev.*, 28, 3291–3302, doi:10.1016/j.quascirev. 2009.09.007.
- Schmiedl, G., and D. C. Leuschner (2005), Oxygenation changes in the deep western Arabian Sea during the last 190,000 years: Productivity versus deepwater circulation, *Paleoceanography*, 20, PA2008, doi:10.1029/2004PA001044.
- Simmonds, I., D. H. Bi, and P. Hope (1999), Atmospheric water vapor flux and its association with rainfall over China in summer, *J. Clim.*, *12*(5), 1353–1367, doi:10.1175/1520-0442(1999)012<1353:AWVFAI>2.0.CO;2.
- Sun, Y., S. C. Clemens, Z. An, and Z. Yu (2006), Astronomical timescale and palaeoclimatic implication of stacked 3.6-Myr monsoon records from the Chinese Loess Plateau, *Quat. Sci. Rev.*, 25, 33–48, doi:10.1016/j.quascirev. 2005.07.005.
- Sun, Y. B., F. Wu, S. C. Clemens, and D. W. Oppo (2008), Processes controlling the geochemical composition of the South China Sea sediments during the last climatic cycle, *Chem. Geol.*, 257(3–4), 243–249.
- Thomson, D. J. (1982), Spectrum estimation and harmonic analysis, *Proc. IEEE*, 70, 1055–1096.Tuenter, E., S. L. Weber, F. J. Hilgen, L. J.
- Tuenter, E., S. L. Weber, F. J. Hilgen, L. J. Lourens, and A. Ganopolski (2005), Simulation of climate phase lags in response to precession and obliquity forcing and the role of vegetation, *Clim. Dyn.*, 24(2–3), 279–295, doi:10.1007/s00382-004-0490-1.
- Uppala, S. M., et al. (2005), The ERA-40 re-analysis, *Q. J. R. Meteorol. Soc.*, *131*(612), 2961–3012, doi:10.1256/qj.04.176.
- Wajsowicz, R. C., and P. S. Schopf (2001), Oceanic influences on the seasonal cycle in evaporation over the Indian Ocean, *J. Clim.*, *14*, 1199–1226, doi:10.1175/1520-0442(2001) 014<1199:OIOTSC>2.0.CO;2.
- Wang, Y. J., H. Cheng, R. L. Edwards, Z. S. An, J. Y. Wu, C.-C. Shen, and J. A. Dorale (2001), A high-resolution absolute-dated Late Pleisto-

- cene monsoon record from Hulu Cave, China, *Science*, 294, 2345–2348, doi:10.1126/ science.1064618.
- Wang, Y. J., H. Cheng, R. L. Edwards, Y. He, X. Kong, Z. An, J. Wu, M. J. Kelly, C. A. Dykoski, and X. Li (2005), The Holocene Asian monsoon: Links to solar changes and North Atlantic climate, *Science*, 308, 854–857, doi:10.1126/ science.1106296.
- Wang, Y. J., H. Cheng, R. L. Edwards, X. G. Kong, X. H. Shao, S. T. Chen, J. Y. Wu, X. Y. Jiang, X. F. Wang, and Z. S. An (2008), Millennial- and orbital-scale changes in the East Asian monsoon over the past 224,000 years, *Nature*, 451, 1090–1093, doi:10.1038/nature06692.
- Webster, P. J. (1987), *The Elementary Monsoon*, pp. 3–32, John Wiley, New York.
- Webster, P. J. (1994), The role of hydrological processes in ocean-atmosphere interactions, *Rev. Geophys.*, *32*, 427–476.
- Webster, P. J., T. N. Palmer, M. yanai, V. Magaña, J. Shukla, and T. Yasunari (1998), Monsoons: Processes, predictability and the prospects for prediction, *J. Geophys. Res.*, 103, 14451–14510.
- Wei, G., W. Deng, Y. Liu, and X. Li (2007), High-resolution sea surface temperature records derived from foraminiferal Mg/Ca ratios during the last 260 ka in the northern South China Sea, *Palaeogeogr. Palaeoclimatol. Palaeoecol.*, 250, 126–138, doi:10.1016/j.palaeo. 2007.03.005.
- Yanai, M., and T. Tomita (1998), Seasonal and interannual variability of atmospheric heat sources and moisture sinks as determined from NCEP-NCAR reanalysis, J. Clim., 11(3), 463– 482.
- Yuan, D. X., et al. (2004), Timing, duration, and transitions of the last interglacial Asian monsoon, *Science*, 304, 575–578.
- Zhu, Y., and R. E. Newell (1998), A proposed algorithm for moisture fluxes from atmospheric rivers, *Mon. Weather Rev.*, 126, 725–735, doi:10.1175/1520-0493(1998)126<0725: APAFMF>2.0.CO;2.
- S. C. Clemens and W. L. Prell, Department of Geological Sciences, Brown University, Providence, RI 02912, USA.
- Y. Sun, SKLLQG, Institute of Earth Environment, Chinese Academy of Sciences, Xi'an 710075, China.